

Eruptive and magma feeding system evolution of Sośnica Hill Volcano (Lower Silesia, SW Poland) revealed from Volcanological, Geophysical, and Rock Magnetic Data

M.S. Petronis^{a, □}, M. Awdankiewicz^b, J. Valenta^c, V. Rapprich^d, J.P. Zebrowski^a, E. Karim^{a, 1}

^a Environmental Geology, Natural Resources Management Department, New Mexico Highlands University, P.O. Box 9000, Las Vegas, NM 87701, USA

^b Institute of Geological Sciences, Wrocław University, pl., Maska Borna 9, 50-204 Wrocław, Poland

^c Faculty of Science, Charles University, Albertov 6, 128 00 Prague 2, Czech Republic

^d Czech Geological Survey, Klárov 3, 118 21 Prague 1, Czech Republic

ARTICLE INFO

Article history:

Received 26 May 2021

Received in revised form 18 July 2021

Accepted 31 July 2021

Keywords:

Monogenetic volcano

Volcano growth

Ground geophysics

Rock magnetics

Sośnica Hill volcano

Bohemian Massif

ABSTRACT

The Sośnica Hill volcano is part of the Oligocene to Miocene (30.9–20.0 Ma) Strzelin volcanic field. It is located 100 km east of the Ohře Rift in the eastern part of the Fore-Sudetic Block, south of the town of Strzelin, Poland. Modern quarrying has exposed the sub-volcanic magma feeder system of the central part of the volcano and an extrusive volcanic succession that includes a 40 m thick sequence of lava flows and pyroclastic deposits that collectively form a complex scoria cone. Geophysical data (ground magnetometry and electric resistivity tomography (ERT)) reveal sharp linear anomalies that are interpreted to reflect normal faults dissecting the volcano. The ERT data map both high and low resistivity bodies, likely representing coherent clay-free dry rocks and partly argillized volcanoclastic deposits, respectively. Paleomagnetic data from 20 intrusive sites reveal two populations of reverse polarity site mean data; 11 sites are of low dispersion and yield a group mean direction that is discordant to the expected field direction, while six sites are highly scattered. Three sites did not yield interpretable results. We interpret the 11 sites as time-averaged field directions that are discordant to the expected field. The high dispersion of the remaining six sites are interpreted to indicate sub-volcanic deformation associated with the growth of the volcanic construct or multiple magma pulses over an extended period of time relative to secular variation. AMS data from 35 sites show a range of flow directions that vary across the quarry without an orderly pattern of fabric orientations. The flow pattern identified from dike paired margin data exhibits sub-vertical upward flow, sub-vertical downward, and moderately inclined northwest flow. Field observations and mapping indicate a complex development of the system in terms of styles of eruptive activity and structure of the final volcanic edifice. The activity included Strombolian and effusive phases, followed by phreatomagmatic, Hawaiian and again effusive eruptions. Such diversity of eruptive styles shows that the origin of the volcano is more complex than a simple, 'textbook' monogenetic scoria cone. Palaeosol on top of Strombolian deposits document a longer break in activity, after which eruptions resumed with different style; this is also not typical of monogenetic cones. The lateral variation in the volcanic succession suggests eruptions from several smaller, local vents. The complex subvolcanic magma flow patterns recorded in dikes match the variation of surface eruptive products and documents dynamically changing magma distribution paths in the near-surface and intra-cone part of the feeding system of the volcano.

© 2021

□ Corresponding author.

E-mail addresses: mmpetro@nmhu.edu (M.S. Petronis),

marek.awdankiewicz@uwr.edu.pl (M. Awdankiewicz),

valentah@natur.cuni.cz (J. Valenta), vladislav.rapprich@geology.cz

(V. Rapprich).

¹ Now at: JFM Environmental Limited, 318 Neptune Crescent, Unit 1, London, ON N6M 1A1, Canada.

<https://doi.org/10.1016/j.jvolgeores.2021.107367>

0377-0273/© 2021

1. Introduction

Scoria cones are the most common type of volcanic landforms on the Earth's continents (Wood, 1980; Cas and Wright, 1987; Schmincke, 2004). They represent one type of monogenetic volcanoes that occur within volcanic fields or as parasitic craters associated with larger complex volcanoes. Mafic monogenetic volcanic fields comprised of tens to hundreds of small cinder cones and craters along with associated lavas

are among the most common manifestations of continental basaltic (*sensu lato* (*s.l.*)) volcanism (Cas and Wright, 1987). Recent studies have shown that scoria cones may be much more complicated than previously thought, in their morphology (e.g. Kereszturi and Németh, 2012), in their deposits (e.g. Németh, 2010), their internal plumbing (Petronis et al., 2013; Delcamp et al., 2014; Petronis et al., 2015; Petronis et al., 2018), petrology of erupted rocks (Rapprich et al., 2017), and variation in eruption style (Chain des Puys, France de Goer et al., 1991; Eifel Volcanic Field, Germany: Sigurdsson et al., 2000; Schmincke, 2004; Lémptegy Volcano, Chain des Puys, France, Petronis et al., 2013; Trosky Volcano, Czech Republic, Petronis et al., 2015; Lunar Crater Volcanic field, Hintz and Valentine, 2012; Cerros del Rio Volcano, New Mexico, USA, Foucher et al., 2018; Paricutin volcano, Luhr and Simkin, 1993; Laghetto scoria cone, Calvari and Pinkerton, 2004). Despite these studies the geometry and dynamics of magma feeders beneath the scoria cones remains poorly understood. The investigation of excavated volcanoes is thus important for understanding the processes driving the magma to generate divergent pathways, secondary vents, and eruptive lava flows away from central vent areas. Here we present results from the basaltic rocks of Sośnica Hill near Targowica, Poland; an Oligocene to Miocene scoria cone. At Sośnica Hill, hereafter referred to as the Targowica quarry, compared to many other remnants of Cenozoic volcanic centers in Central Europe, this volcano is exceptionally well preserved, as the degree of erosion was relatively limited and it was also partly buried by sequences of post-eruptive sedimentary rocks, and recent quarrying has revealed the subvolcanic roots of the volcanic system along with the surface volcanic facies. The site is located in the Fore-Sudetic Block in the eastern part of the Cenozoic Central European Volcanic Province. The volcanic succession at Targowica quarry is mined to over 50 m depth revealing pyroclastic deposits, subvolcanic intrusions, lobate-, aa- and pahoehoe- type lava flows. The purpose of this research is to use field observations, geophysical, paleomagnetic, and AMS data to reconstruct the outer cinder cone morphology, eruptive dynamics, magma plumbing system geometry, evolution of sub-volcanic deformation, and magma flow patterns.

2. Geologic setting

The northern part of the Circum-Mediterranean Volcanic Province (Lustrino and Wilson, 2007) is known as the Central European Volcanic Province (CEVP). Variably eroded central volcanic complexes (e.g., Wilson et al., 1995; Rapprich and Holub, 2008; Cajz et al., 2009; Holub et al., 2010; Skála et al., 2014) as well as mafic monogenetic volcanic fields (e.g., Mertes and Schmincke, 1985; Awdankiewicz, 2005, 2013; Rapprich et al., 2007; Büchner and Tietz, 2012; Büchner et al., 2015; Tietz and Büchner, 2015), often associated with rift zones, are characteristic of the CEVP (Wilson and Downes, 1991, 2006) Basaltic volcanism in the CEVP and namely in the Bohemian Massif are generally linked with lithospheric extension and melting of upwelling asthenosphere with variable interactions between the melts of asthenospheric and lithospheric origin. However, a number of different petrogenetic models have been proposed to account for the causes of mantle melting, the variable mantle sources involved, and their variation in space and time (Lustrino and Wilson, 2007).

The Bohemian Massif located in present day Poland, Czech Republic, Austria, and Germany represents one of the largest remnants of the Variscan orogeny (continental collisional belt between Laurasia and Gondwana, 360 Ma - 325 Ma: Matte, 1986). The highest frequency of volcanic rocks occur within the Eger Rift, an extensional graben cross-cutting the northwestern part of the Bohemian Massif from southwest to northeast. The Eger Rift follows a Variscan suture zone between the Saxothuringian domain in the northwest and the Moldanubian and Teplá-Barrandian domains in the southeast (e.g., Babuška and Plomerová, 2001; Mlčoch and Konopásek, 2010; Fig. 1A). Numerous volcanic fields in the Bohemian Massif occur also off the Eger Rift axis,

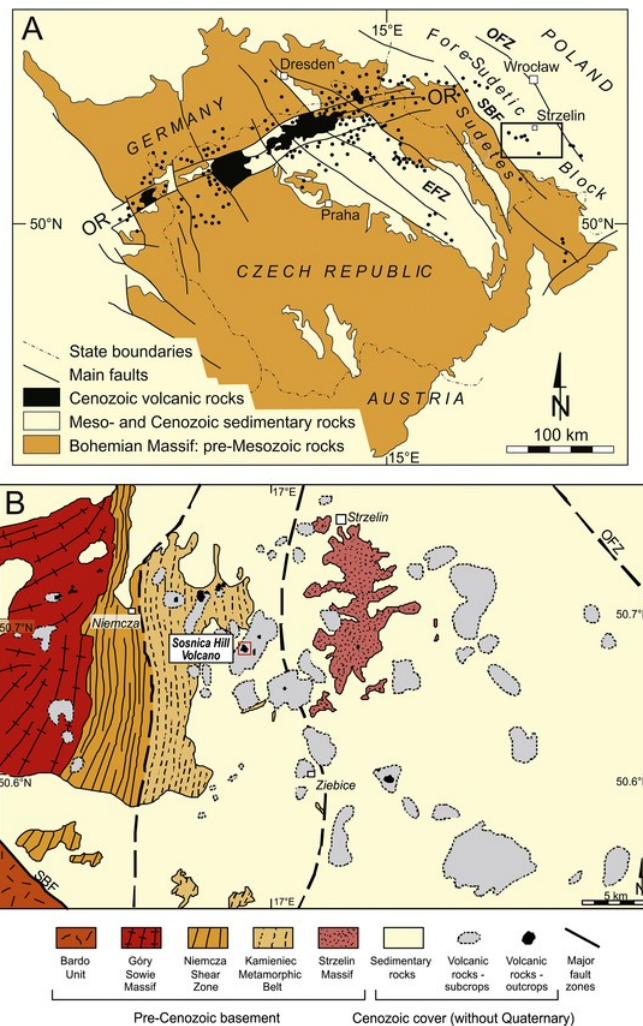


Fig. 1. Geological sketch maps of the study area. **1A)** Location of the Strzelin Volcanic Field (black frame) within the Bohemian Massif (modified from Holub et al., 2010). **1B)** Location of the Sośnica Hill volcano in the Strzelin Volcanic Field (modified from Awdankiewicz et al. (2016), based on Sawicki (1967), Cwojdzński and Jodłowski (1982), and Mazur et al. (2006)). EFZ - Elbe Fault Zone, OR - Ohře (Eger) Rift, OFZ - Odra Fault Zone, SBF - Sudetic Boundary Fault.

up to 150 km away from its edges. The Sudetes and the Fore-Sudetic Block, east of the Eger Graben (Fig. 1A) feature scattered remnants of mafic, monogenetic volcanoes. There are over 300 outcrops of Cenozoic basaltic rocks with the majority occurring as plugs or lava flows (Awdankiewicz, 2005 and references therein). The volcanic rocks are mostly basanites and tephrites, more rarely nephelinites and alkali basalts with isolated outcrops of trachytes and latites (Awdankiewicz, 2005; Kozłowska-Koch, 1987). The volcanic activity in this region spanned from Late Oligocene to Pliocene based on K-Ar age determinations that yield ages 30.9 Ma to 3.8 Ma (Birkenmajer and Pécskay, 2002; Birkenmajer et al., 2002a, 2002b, 2004). Our study area (Fig. 1B) is located 100 km east of the Eger Rift, in the Strzelin-Ziębice Volcanic Field (SZVF; Awdankiewicz et al., 2016).

3. Targowica quarry

In the study area, in the central part of the SZVF (Fig. 1B), there are three basaltic volcanic and volcanoclastic rock outcrops with two small poorly exposed outcrops located east of the Targowica village and the well exposed Targowica quarry located on Sośnica Hill (16.97°E, 50.69°N; Fig. 1B). The Miocene Targowica basalts are dated at

23–20 Ma (Birkenmajer et al., 2004). The basalts are exposed in a quarry operating with periodic breaks since the early-20th Century (Fig. 2). At the time of an earlier study (Awdankiewicz, 2005), the quarry was abandoned and ~ 120 m × 350 m in size. Pyroclastic fall deposits (mainly scoria breccias), subvolcanic intrusions (a plug, dykes and other intrusive sheets) and aa-type lavas were identified. This suc-

cession was linked to the activity of a Strombolian scoria cone (the Sośnica Hill volcano). Initial Hawaiian to Strombolian-type explosive eruptions produced a pyroclastic cone. Subsequently subvolcanic intrusions and lavas were emplaced. The lavas were fed from the central vent of the volcano, and breached the cones flank and flowed southwards. Later eruptions resumed at a new vent on the western slopes of

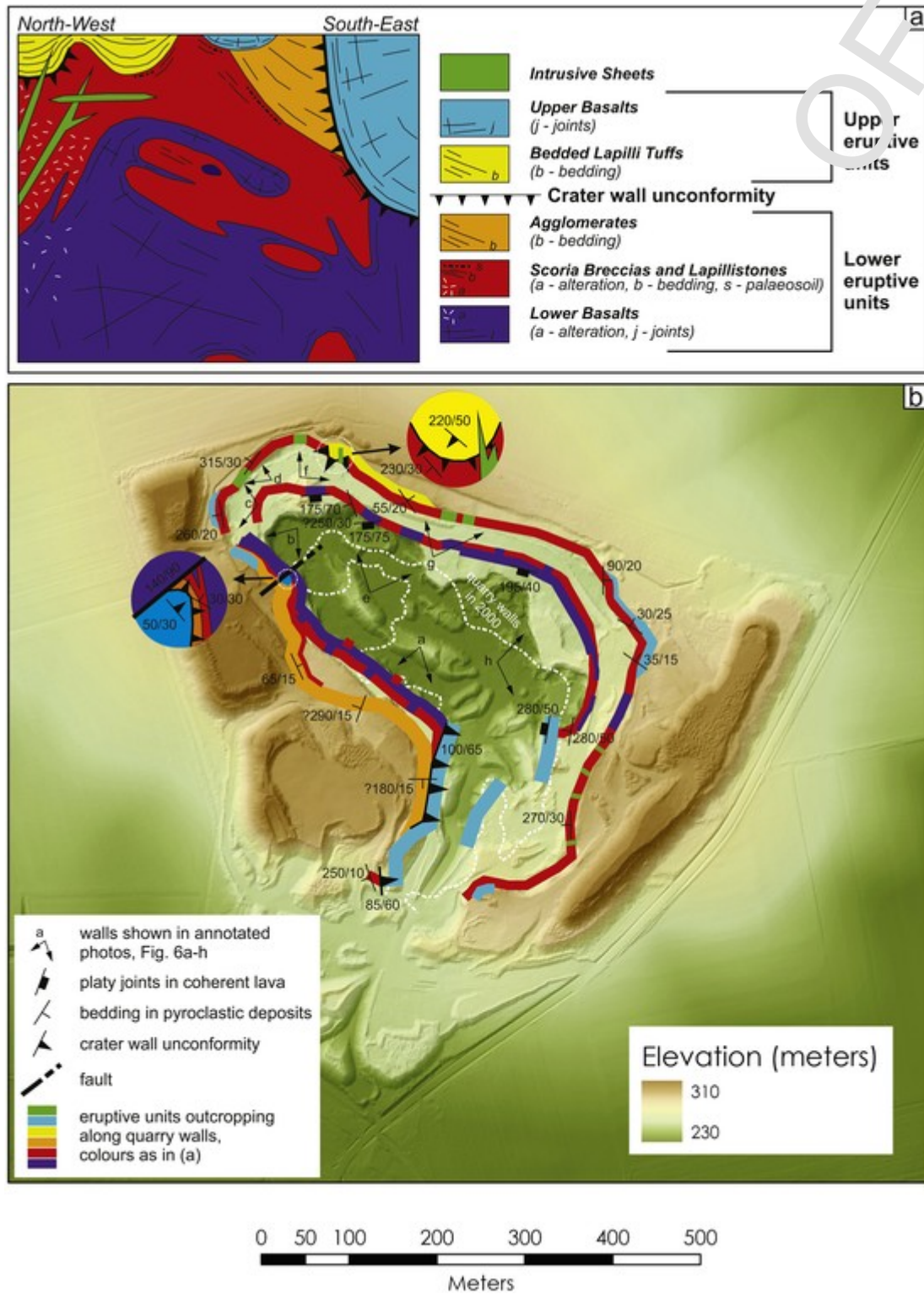


Fig. 2. Geology of the Targowica Quarry Area.

2A) Stratigraphic log showing idealized relationships between eruptive units. **2B)** Geological sketch map showing the eruptive units outcropping along quarry walls as in 2016.

the main cone (Awdankiewicz, 2005). The original edifice was inferred to be 500 m – 1000 m in basal diameter and 90 m – 180 m high, with the main crater located N-NE of the quarry, a smaller vent on the western slope, and lava-filled breach in the south. It was concluded that since its formation 23–20 Myr ago, the original edifice was substantially eroded, down to ~1/2 of the height and 1/8 of the volume of the original cone (Awdankiewicz, 2005). However, most other volcanoes in Lower Silesia region are much more strongly eroded: the surface volcanic facies almost totally removed, and only deeper subvolcanic facies are exposed (e.g. Migoń and Pijet-Migoń, 2016). Previous work at Targowica quarry (Awdankiewicz, 2005; Awdankiewicz et al., 2016) have shown that the basalts are uniform in terms of bulk-rock chemistry and petrography, with some minor variation related to 1) different cooling rates of, e.g. lavas vs. pyroclastic materials, as well as to 2) alteration and weathering; these aspects, however, are beyond the scope of the present study.

In 2010, the quarry was reopened and, over the next few years, the quarry progressed by 100 m – 150 m in the W, N and E directions, as well as few tens of meters downwards. In 2016, when the new study was conducted, the quarry was ~500 m × 250 m in lateral extent and ~ 60 m – 70 m in depth. The widened exposure revealed lithologies not recognized previously, as well as more complex structures, calling upon revision and update of previous observations. The new field

data, together with geophysical measurements, suggest a more complex evolution of Sońnica volcanic system (such as more diversified styles of explosive, effusive and intrusive activity), and constrain more precisely the location of vents and feeders and magma movements in the shallow subsurface part of the volcanic system.

4. Methods

4.1. Field work

This study commenced with field work focused at mapping, logging and textural characterization of the volcanic facies. A geological map of the quarry was compiled that depicts the structures of the volcanic succession and textures of the various facies are illustrated in several annotated plates (Fig. 2 and Fig. 3).

4.2. Sampling methods

Paleomagnetic sampling involved collecting eight to ten drill core samples at twenty sites (Table 1) while anisotropy of magnetic susceptibility (AMS) sampling involved collecting samples at thirty-two sites (Table 2). The AMS sites were collected from the same dikes sampled for paleomagnetic analysis but with additional sites collected along

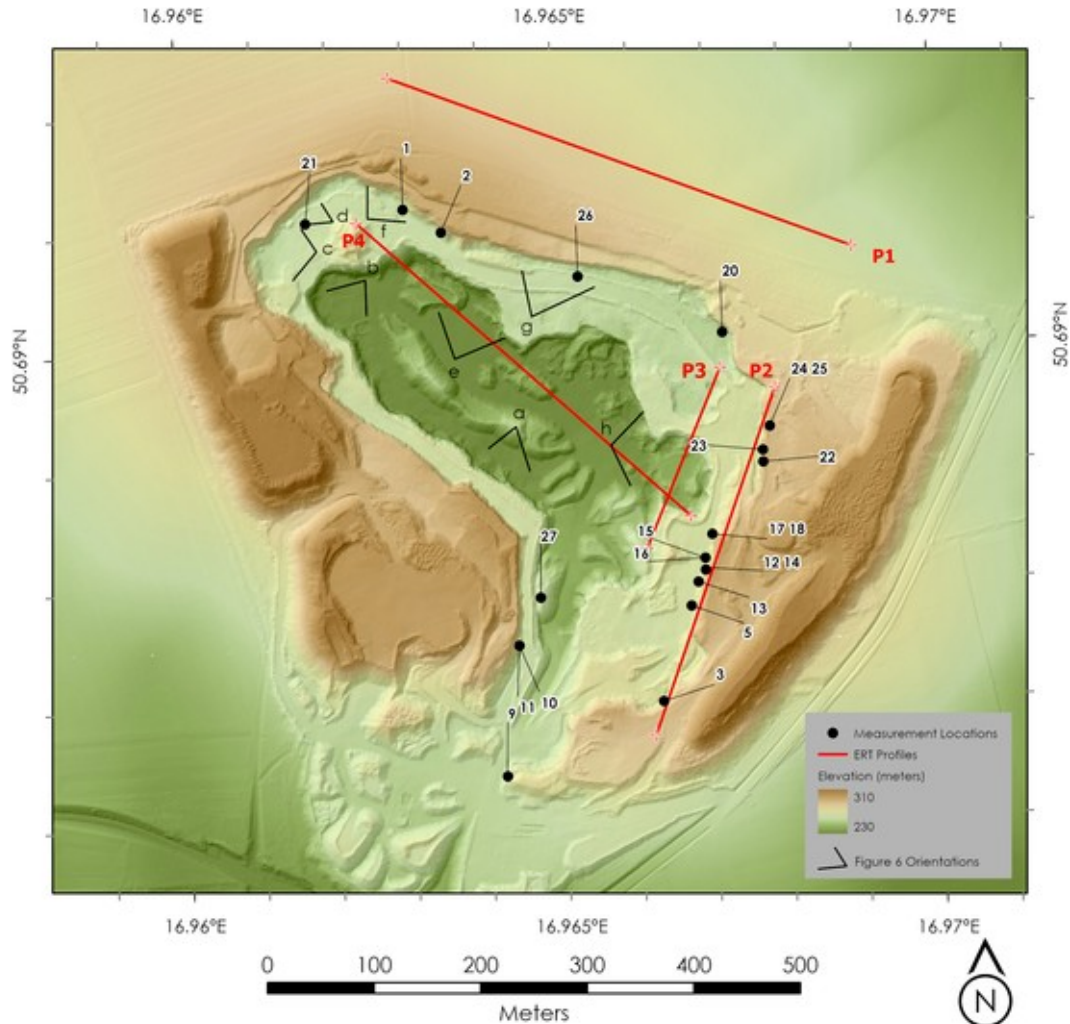


Fig. 3. Sampling sites and electrical resistivity profile locations.

Digital elevation model of the Targowica quarry showing location of paleomagnetic - anisotropy of magnetic susceptibility sampling locations, the position of the ERT profile sections (red lines), and annotated field photographs shown in Fig. 6. (For interpretation of the references to color in this figure legend, the reader is referred to the web version of this article.)

Table 1

Paleomagnetic data from the Targowica quarry, Lower Silesia, SW Poland.

Site	N/No	R	α_{95}	k	Dec	Inc	VGP Lat (N)	VGP Long (W)	Longitude (°E)	Latitude (°N)	
Tvq 1	7/7	6.84	10.1	36.75	174.0	-64.3	83.9	299.2	16.9630	50.6912	
Tvq 2	6/7	5.98	4.4	234.76	342.9	-46.8	9.9	147.7	16.9635	50.6910	
Tvq 3	7/7	6.96	4.8	159.57	269.9	-61.5	31.6	103.2	16.9663	50.6870	
Tvq 5*	reject - no stable end point									16.9667	50.6878
Tvq 9	6/7	6.56	6.0	124.30	185.9	-67.3	86.2	67.5	16.9642	50.6864	
Tvq 10	4/7	3.98	7.9	137.90	067.9	-65.9	24.6	205.8	16.9644	50.6875	
Tvq 11*	6/6	4.61	24.9	10.37	203.1	-61.4	72.3	54.8	16.9644	50.6875	
Tvq 12	7/7	6.95	5.4	125.39	212.2	-61.1	66.5	64.6	16.9669	50.6881	
Tvq 13	6/7	5.89	10.0	46.24	203.8	-61.7	72.1	56.8	16.9668	50.6880	
Tvq 14	6/6	5.91	8.9	57.81	225.0	-66.7	61.4	88.1	16.9669	50.6881	
Tvq 15*	3/3	2.96	18.2	47.15	306.1	-55.3	8.6	121.5	16.9669	50.6882	
Tvq 16	3/3	2.99	5.1	583.64	077.9	-40.0	10.2	229.3	16.9669	50.6882	
Tvq 17 18	6/7	5.91	9.1	54.62	192.3	-66.1	81.7	62.7	16.9670	50.6884	
Tvq 20	6/7	5.96	5.4	141.96	177.5	-82.2	65.9	164.6	16.9672	50.6901	
Tvq 21	5/5	4.97	6.4	144.47	331.8	-72.8	21.3	147.5	16.9617	50.6911	
Tvq 22	6/6	5.98	3.7	325.45	196.2	-75.9	74.6	134.9	16.9677	50.6890	
Tvq 23	7/7	6.87	9.1	44.61	184.7	-68.7	86.7	101.2	16.9677	50.6891	
Tvq 24 25	7/7	6.93	6.8	80.00	193.3	-69.7	81.3	97.7	16.9678	50.6893	
Tvq 26	5/6	4.98	5.3	206.64	308.3	-64.5	16.7	128.6	16.9653	50.6906	
Tvq 27	5/6	4.99	3.8	411.67	201.6	-66.0	75.8	72.1	16.9647	50.6879	
		N/No	R	α_{95}	k	Dec	Inc	VGP (k)	VGP (s)		
Group Mean Accepted		17/20	15.39	11.9	10.00	206.9	-80.4	4.6	38.0		
Eleven Clustered Sites		11/20	10.89	4.7	87.2	196.6	-68.8	37.8	13.1		

Paleomagnetic data from the studied samples. Site-paleomagnetic sampling location; N/No- number of samples used (N) from the actual number of samples collected (No) at each site; R- resultant vector length; α_{95} - 95% confidence interval about the estimated mean direction, assuming a circular distribution, k -best estimate of Fisher precision parameter; Dec/Inc- in situ declination and inclination; VGP lat/long- latitude and longitude of the virtual geomagnetic pole for each site; Longitude and Latitude of the sampling site; VGP (k), group mean precision parameter; VGP (s), group mean angular dispersion estimate where $s = 81^\circ/\sqrt{k}$.

paired margins and the center of the dikes, thus increasing the total number of sampling sites for AMS analysis. All samples were collected with either a modified Echo 280E gasoline powered drill with a non-magnetic diamond tip drill bit or collected as oriented block samples (Fig. 3). All drill core samples were oriented in situ with a Pomeroy orienting device using a magnetic and, when possible, a sun compass. Block samples were oriented using a Brunton compass. At each drill site, independent core samples were obtained from along the margins and/or across the center of the intrusions with the total number of samples collected at each site dependent upon the level of exposure. At four dikes, we were able to sample along paired margins (Table 2) given favorable outcrop exposure with the remaining intrusions sampled along at least one margin and/or in the center of the planer intrusion. All core samples were cut into 2.2 cm by 2.5 cm right-cylinder specimens, using a diamond tipped, non-magnetic saw blade with up to three specimens per core sample obtained at the New Mexico Highlands University's Rock Processing laboratory. Sample site locations were precisely located using a Garmin GPS 60Csx. To characterize the magnetic mineralogy, we conducted a suite of laboratory experiments with the goal of identifying the magnetic phases carrying the remanence, and the overall ability of these rocks to faithfully record an ambient magnetic field. All experiments were conducted at the New Mexico Highlands University Paleomagnetic-Rock Magnetic laboratory, USA. Equipment used included an AGICO JR6A dual-speed spinner magnetometer, 2G Enterprise Superconducting Rock Magnetometer Model 755-4 K System, home-built and ASC Scientific (Model IM-10-30) static impulse magnets capable of 1 to 3 Tesla peak fields. All AMS, susceptibility, and Curie point experiments were measured with an AGICO MFK1-A kappabridge susceptibility meter with a CS4 high temperature attachment operating at low alternating field of 200 A/m at 976 Hz. All hysteresis and first order reversal curve (FORC) measurements were conducted on a Lake Shore Cryotronics Vibrating Sample Magnetometer Model 8600.

4.3. Geophysical field methods

Ground geophysical methods provide a useful tool for imaging the internal structure of volcanoes (e.g., Skácelová et al., 2010; Bolós et al., 2012; Blaikie et al., 2012, 2014; Schmidt et al., 2013; Valenta et al., 2014a, 2014b; Flechsig et al., 2015; Marshall et al., 2015). Geophysical tomography studies of monogenetic pyroclastic cones are rather scarce and focus mostly on Quaternary volcanoes (e.g., Peccerillo et al., 2006; Finizola et al., 2010; Barde-Cabusson et al., 2013; Bolós et al., 2014). The interior of the Targowica quarry was imaged by electrical resistivity tomography (ERT; e.g. Loke and Barker, 1996; Oldenburg and Yaoguo, 1999; Udphuay et al., 2011, Torrese et al., 2021) and ground magnetometry (Fig. 3). The normal magnetic field in the area according to the World Magnetic Model (Chulliat et al., 2015) should be about 49,600 nT. The field magnetic data were acquired using the PMG-2 Proton precession magnetometer (SatisGeo, Ltd.). The measured data were corrected for the diurnal variations of the geomagnetic field based on repeat base station measurements. The recorded variations (33 nT) were much smaller than changes of the total field within the locality (more than 3000 nT). The measured magnetic field was visualized in a form of a contour map (Fig. 4A). The ERT data were measured on profiles 1, 2, 3 and 4 (Fig. 4B) using the ARES resistivity meter (GF Instruments, Ltd.). The electrode array used was the Wenner-Schlumberger array (e.g., Reynolds, 2011) and the electrode separation on all profiles was 5 m. The average error of field measurements based on the repeated readings (four to eight readings for each measured point, based on the voltage differences measured) was 0.17% and maximum measured error was 4.9%. Individual profiles were processed using a standard 2D inversion technique using the BERT program (Rücker et al., 2006; Gunther et al., 2006; Fig. 4B).

4.4. Paleomagnetic methods

Remanent magnetizations of all samples were measured at the New Mexico Highlands University Paleomagnetic-Rock Magnetic laboratory.

Table 2

Anisotropy of magnetic susceptibility data from Targowica quarry, Lower Silesia, SW Poland.

Sites	Sub-sites	No	Km E-3 (SI)	K1	K2	K3	K1-K2	F	L	Pj	T			
TVQ 1	A	Paried Margin	6	25.6	162/01	252/24	068/66	158	#	W	1.007	1.007	1.013	-0.020
	B	"	11	23.7	187/12	280/10	048/74	138	#	W	1.007	1.007	1.014	0.020
	C	"	5	10.2	319/02	050/20	224/70	314	#	N	1.011	1.003	1.015	0.479
	D	"	13	12.8	081/36	316/38	197/31	287	#	N	1.008	1.005	1.014	0.125
TVQ 5	A	Paried Margin	14	13.6	012/14	274/31	123/56	213	#	W	1.007	1.006	1.013	0.084
	B	"	6	15.4	188/04	097/10	301/79	031	#	E	1.008	1.006	1.014	0.098
	C	"	6	10.4	126/50	255/28	000/26	090	#	S	1.004	1.003	1.007	0.122
TVQ 6	A	Paried Margin	9	22.9	290/51	061/28	165/24	255	#	N	1.005	1.003	1.008	0.225
	B	"	8	31.2	204/54	330/23	072/26	162	#	W	1.003	1.002	1.006	0.164
TVQ 8	A	Paried Margin	7	29.0	293/64	048/12	143/23	233	#	N	1.002	1.001	1.004	0.191
	B	"	6	14.3	246/30	019/49	141/25	231	#	N	1.006	1.003	1.009	0.274
TVQ 2	A		8	38.4	006/05	100/34	269/57	359	#	E	1.006	1.004	1.010	0.212
TVQ 3	A		17	24.1	073/29	319/35	192/41	282	#	N	1.014	1.006	1.021	0.421
TVQ 9	A		8	29.5	295/38	076/44	188/21	278	#	N	1.015	1.007	1.023	0.307
TVQ 10	B		13	10.3	163/44	032/34	282/27	012	#	E	1.009	1.005	1.015	0.269
TVQ 11	A		6	10.5	327/33	081/33	204/40	294	#	N	1.011	1.008	1.019	0.133
TVQ 12	A		9	18.7	101/50	254/38	354/38	084	#	S	1.002	1.002	1.004	0.215
TVQ 13	A		8	16.1	315/28	139/62	046/02	136	#	W	1.005	1.005	1.011	-0.106
TVQ 14	A		10	17.9	175/15	075/32	286/54	016	#	E	1.004	1.005	1.009	-0.178
TVQ 15	C		6	38.3	359/31	100/18	215/53	305	#	N	1.003	1.007	1.010	-0.435
TVQ 16	A		13	22.0	350/32	214/49	096/23	186	#	W	1.005	1.011	1.017	-0.364
TVQ 17	A		8	19.8	082/14	333/53	182/34	272	#	N	1.004	1.007	1.012	-0.259
Sites	Sub-sites	No	Km E-3 (SI)	K1	K2	K3	K1-K2	F	L	Pj	T			
TVQ 18	A	13	22.4	278/08	013/31	174/58	264	#	N	1.019	1.005	1.026	0.563	
TVQ 19	A	9	11.9	174/18	272/24	050/60	140	#	W	1.004	1.003	1.008	0.338	
TVQ 20	A	8	12.0	185/34	007/56	2766/01	006	#	E	1.005	1.002	1.008	0.498	
TVQ 21	A	12	28.1	178/50	085/02	354/40	084	#	S	1.007	1.006	1.012	0.052	
TVQ 22	A	11	44.3	331/22	228/29	092/52	182	#	W	1.015	1.005	1.022	0.500	
TVQ 23	A	8	42.1	337/09	199/78	069/08	159	#	W	1.014	1.005	1.019	0.399	
TVQ 24	A	9	48.9	139/37	353/47	243/18	333	#	E	1.009	1.009	1.018	0.011	
TVQ 25	A	7	49.4	145/30	271/46	036/29	126	#	S	1.007	1.018	1.026	-0.459	
TVQ 26	A	9	26.4	051/22	319/07	213/67	303	#	N	1.004	1.006	1.010	-0.289	
TVQ 27	A	7	16.8	345/16	211/68	080/15	170	#	W	1.009	1.010	1.019	-0.085	

Sites, site location name; Sub-sites, sites collected along the margins or center of the intrusion; No, number of specimens analyzed at each site; K_m , mean susceptibility; K_1 , magnetic lineation = long axis of the magnetic susceptibility ellipsoid; K_2 , intermediate axis; K_3 , normal to the magnetic foliation plane; K_1-K_2 plane, is normal to minimum susceptibility axis; F, ratio of K_2/K_3 ; L, Ratio of K_1/K_3 ; P_j , corrected anisotropy degree; T, shape parameter. See **Table 1** for site coordinates.

Specimens were progressively alternating field (AF) demagnetized, typically in 10 to 25 steps, to a maximum field of 120 mT using an ASC Scientific D-TECH 2000 AF-demagnetizer or integrated AF system. Samples with high coercivity were treated with thermal demagnetization (TH) up to a maximum of 630 °C, yet with most samples being fully demagnetized by 580 °C. Thermal demagnetization experiments on replicate specimens, to compare with AF behavior, were conducted with an ASC Scientific TD48 thermal demagnetizer. Principal component analysis (PCA; Kirschvink, 1980) was used to determine the best-fit line through selected demagnetization data points for each sample using Remasoft 3.0 (Chadima and Hrouda, 2006) (Fig. 5; Table 1). For most samples, a single best-fit line could be fit to the demagnetization data points. Best-fit magnetization vectors involved 5 to 18 data points, but as few as 3 to as many as 25 were used, and for less than 10% of the samples it was necessary to anchor them to the origin. Magnetization vectors with maximum angular deviation values greater than 5° were not included in site mean calculations.

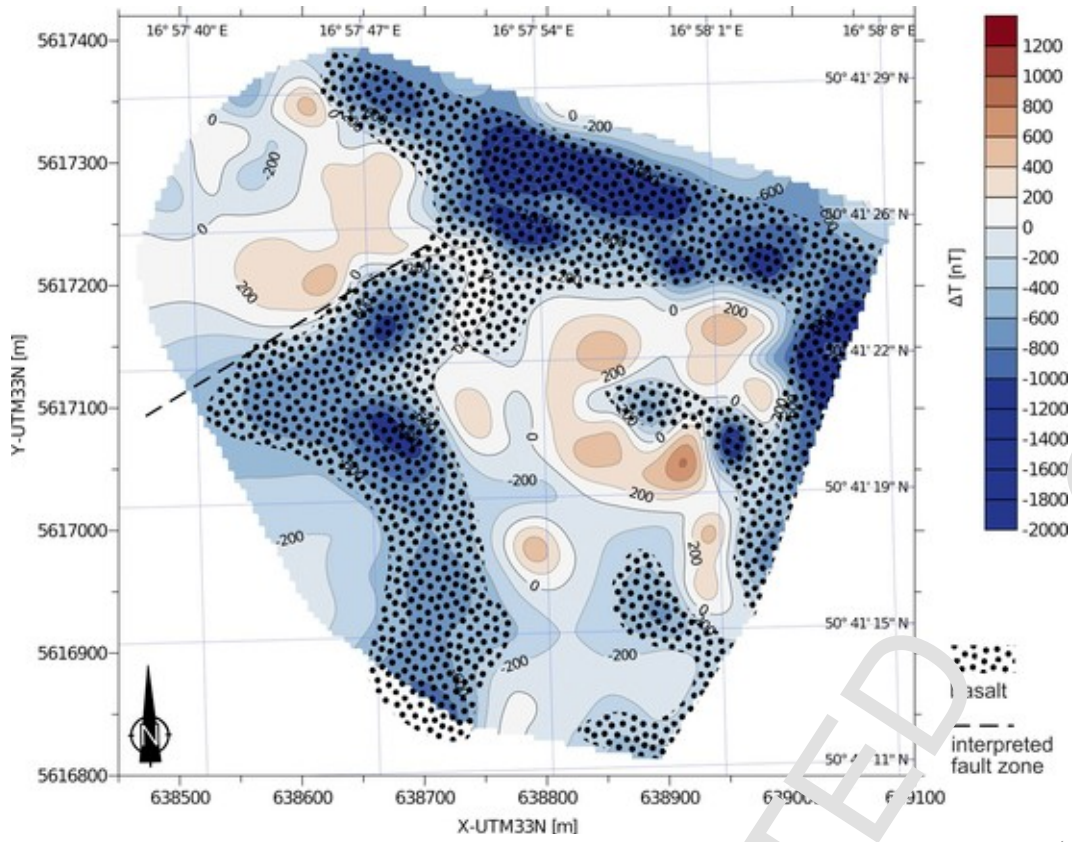
4.5. Anisotropy of magnetic susceptibility methods

Anisotropy of magnetic susceptibility (AMS) measurements of a rock specimen yields an ellipsoid of magnetic susceptibility (K) defined by the length and orientation of its three principal axes, $K_1 \geq K_2 \geq K_3$, which are the three eigenvectors of the susceptibility tensor (Tarling and Hrouda, 1993). The long axis of the magnetic susceptibility ellipsoid, K_1 , defines the magnetic lineation, while the short axis, K_3 , defines the normal to the magnetic foliation plane (K_1-K_2). The bulk magnetic

susceptibility (K_m) is the arithmetic mean of the principal axes K_1 , K_2 and K_3 . In addition, the AMS technique defines the degree of magnitude of the linear ($L = K_1/K_2$) and planar ($F = K_2/K_3$) fabric components. The technique also quantifies the corrected degree of anisotropy, $P_j = \exp. (2[(\eta_1 - \eta)^2 + (\eta_2 - \eta)^2 + (\eta_3 - \eta)^2]^{1/2})$, where $\eta_1 = \ln K_1$, $\eta_2 = \ln K_2$, $\eta_3 = \ln K_3$, and $\eta = \ln (K_1 + K_2 + K_3)^{1/3}$. A value of $P_j = 1$ describes a perfectly isotropic fabric, a P_j value of 1.15 describes a sample with 15% anisotropy and so on. Following the above, P_j values of 0–5% indicate a weak anisotropy, 5–10% moderate anisotropy, 10–20% a strong anisotropy, and > 20% a very strong anisotropy. The shape of the susceptibility ellipsoid (T) (with $T = (2\ln k_2 - \ln k_1 - \ln k_3) / (\ln k_1 - \ln k_3)$) (Jelinek, 1981) ranges from +1 where purely oblate to -1 where purely prolate, and is triaxial near zero. We measured the AMS of 290 specimens prepared from samples collected at 32 sites distributed within the Targowica quarry using an AGICO MFK1-A operating at 200 A/m at 976 Hz (Table 2).

4.6. Rock magnetism

Rock magnetic experiments were conducted to better understand the origin of the NRM and the magnetic material that carries the magnetic fabric in these rocks. This project used Curie point estimates, the Lowrie-Fuller test, room-temperature hysteresis loops, room-temperature FORC distributions, and acquisition of isothermal remanent magnetization (IRM) (Dunlop and Özdemir, 1997). Curie point experiments are used to establish the dominant magnetic mineral phase (s) present in the sample and to define, if present, the composition of



(caption on next page)

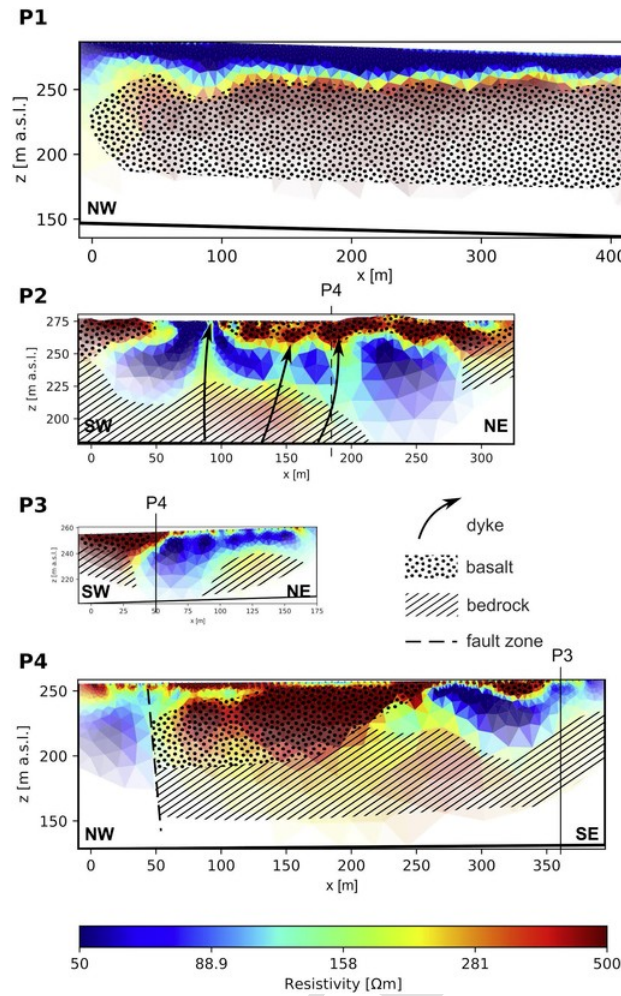


Fig. 4. Geophysical results - ERT and magnetics.

4A: The 2D inversion of individual ERT profiles with location plotted in Fig. 3. The high-resistivity areas (over ca 300 Ωm) could be considered as coherent basic lava flows or intrusions. The exception are the near-surface anomalies (depths of first few meters) where the increased resistivity is more likely an effect of (i) dry and fractured rocks exposed to atmospheric weathering and/or (ii) layers of gravels used to fill and level the depressions in the quarry floor. **4B: Total field deviations of magnetic field measured at the Targowica quarry.** Increased levels of geomagnetic field (more than 200 nT) corresponds to outcrops of coherent basic lavas. The large magnetic minima (less than -1000 nT) in the north part of the area suggests a large body of basic lava of reverse polarity remanent magnetization located to the north (off the measured area).

the titanomagnetite phase(s). The procedure was performed in steps of heating and cooling from 25 °C to 700 °C and back to 40 °C in an Argon atmosphere to minimize oxidation of the sample using a CS4 furnace attachment for the MFK1-A at a rate of ~ 14 °C/min. Methods used for interpretation of Curie points were the inflection point method (Tauxe, 1998) and Hopkinson peak method (Hopkinson, 1889; Moskowitz, 1981). The most common magnetic minerals in igneous rocks and their respective Curie point temperatures include magnetite 575–585 °C, hematite 680 °C, and pyrrhotite 320 °C. The Lowrie-Fuller test (Lowrie and Fuller, 1971) is used to determine the magnetic domain state of the dominate magnetic mineral phase present in the sample (e.g., single domain (SD), pseudo single domain (PSD), multidomain (MD)). The experiment involves demagnetizing the natural remanent magnetization (NRM), anhysteretic remanent magnetization (ARM), and saturation IRM (SIRM). The median destructive field (MDF) represents the field intensity required to remove half of the magnetization. The intensity of the MDF varies according to the composition and domain state of magnetic phase present. The energy required to demagnetize a MD grain is lower than the energy required to demagnetize a SD grain, thus this experiment provides information on the domain state of the magnetic phases present on the sample. All hysteresis and first order reversals curve (FORC) were collected with a Lake Shore Cryotronics Vibrating

Sample Magnetometer Model 8600 (Pike et al., 1999; Roberts et al., 2000). Data collection used the MicroMag 2900/3900 software version 1.3 with a maximum applied field of 2.03 Tesla and field step size of 10 mT. The averaging time was 300 ms, data smoothing factor (SF) was minimum for all samples ($SF = 4$) given the high signal to noise ratio. Final processing of the hysteresis data were prepared in Microsoft Excel and the FORC distributions were generated using the IgorPro Version 8.0.4.2 (WaveMetrics Inc.) software. The number of first-order reversal curves varied between samples from 101 to 137 FORCs per sample to construct a FORC distribution diagrams. To further characterize the domain state of the magnetic mineral(s), we conducted isothermal remanent magnetization (IRM). IRM acquisition experiments often define the composition and the magnetic grain size of the ferromagnetic mineral(s) that are responsible for carrying the remanence and the stability of the magnetization (Dunlop, 1972; Dunlop, 1973; Dunlop, 1981; Butler, 1992). These experiments involve 17–20 magnetization steps to a peak field of 2.5 T or until saturation is reached. The shape of the IRM acquisition curves aids with identifying the grain composition (e.g., titanomagnetite, titanomaghemite, hematite), the magnetic grain size, and the domain state of the dominant magnetic mineral phase(s) present.

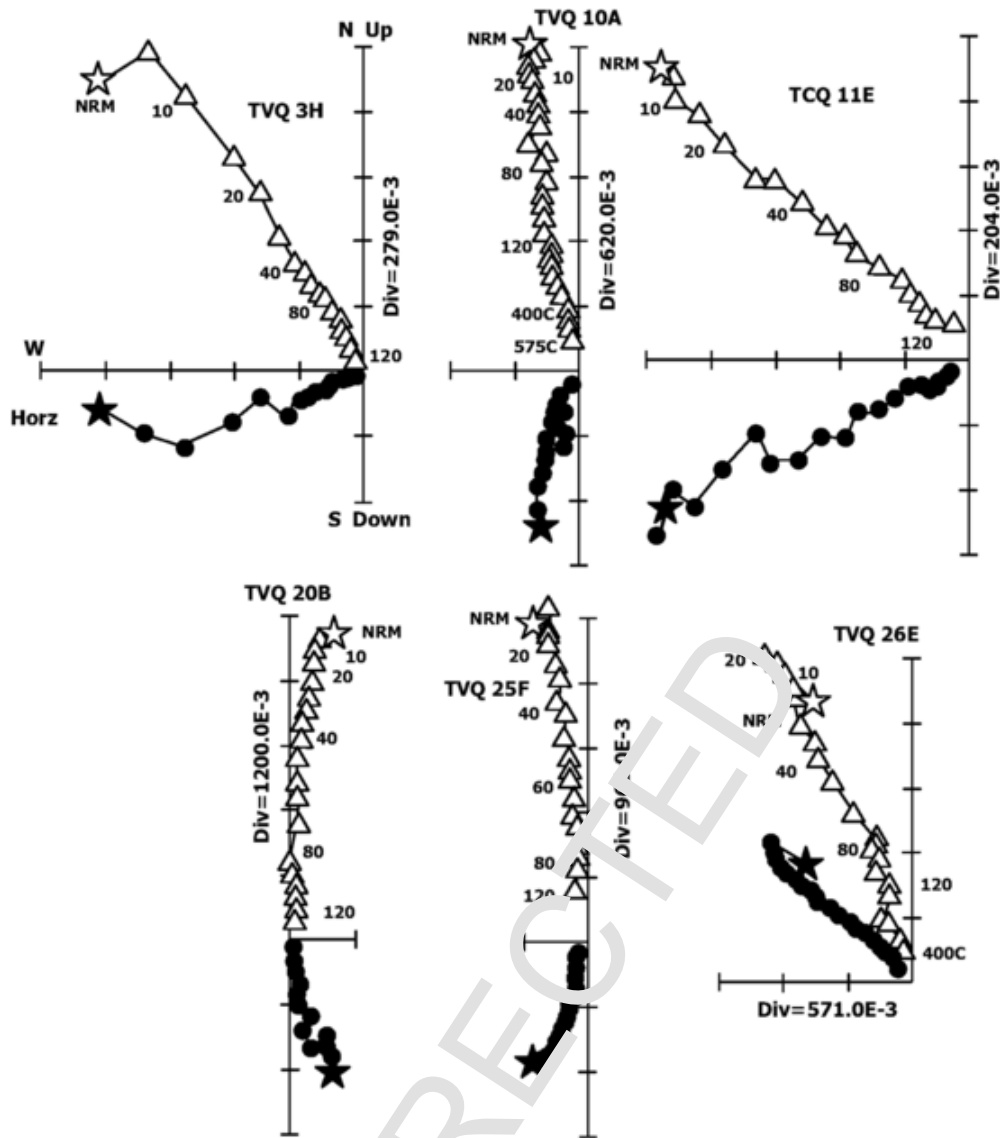


Fig. 5. Orthogonal demagnetization diagrams.

Orthogonal demagnetization diagrams from representative samples from the Targowica quarry showing the typical AF demagnetization behavior (Zijderveld, 1967). Solid (open) symbols represent the projection onto the horizontal (vertical) plane. The demagnetization steps are given in mT and/or in degrees Celsius. Magnetization (in A/m) is shown along one axis for each sample; each division equals indicated intensity.

5. Results

Field Relations at Targowica Quarry

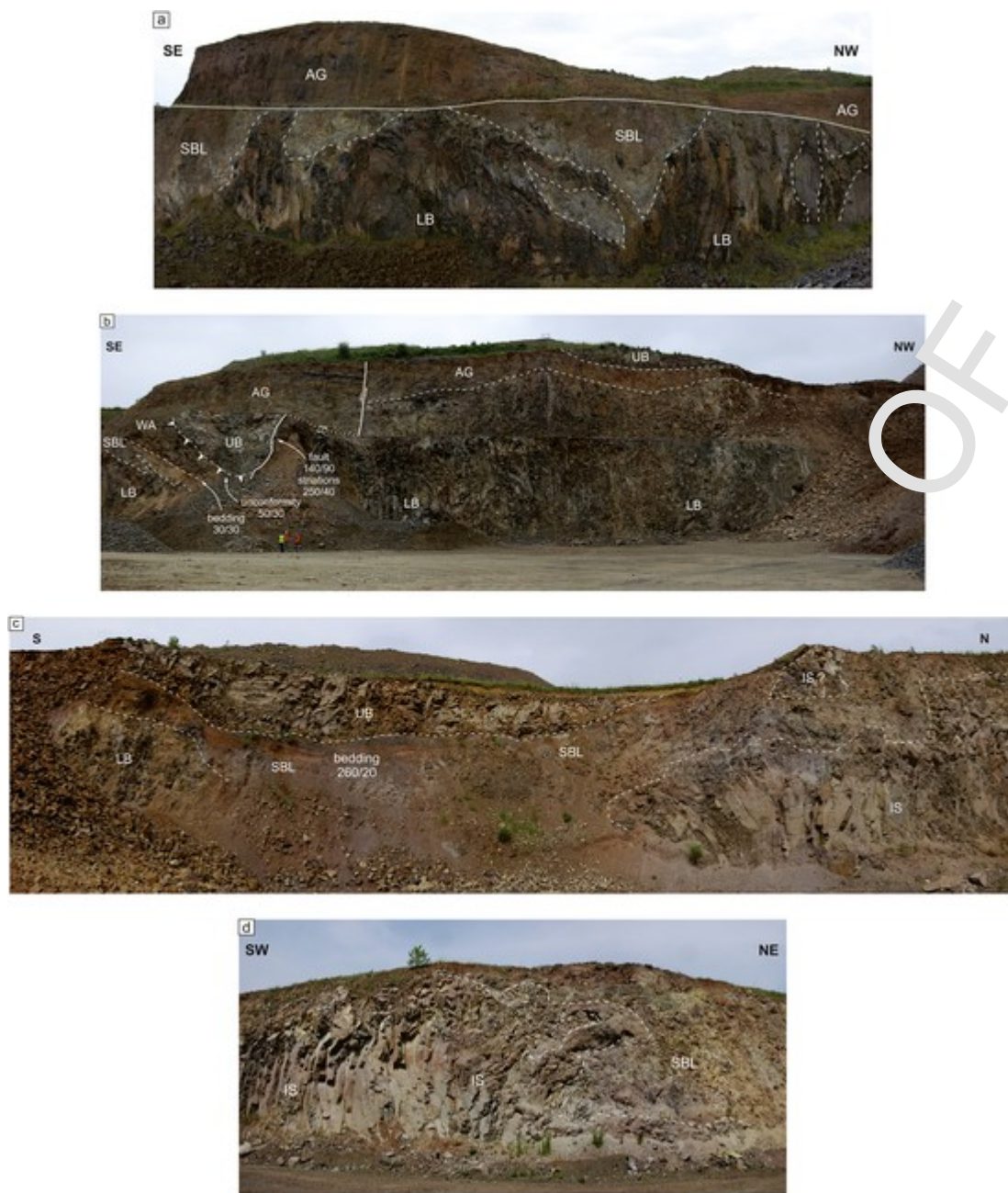
5.1. Eruptive units

Based on depositional structures, lithology and textures, the volcanic succession exposed at Targowica quarry is subdivided into six units, including five eruptive units and one intrusive unit (Fig. 2a). A paleosol horizon as well as a crater wall unconformity are recognized. The unconformities enable distinction of lower eruptive units (below the unconformity) and upper eruptive units (above the unconformity). A geological sketch map of the quarry (Fig. 2b) and series of annotated panoramic photos (Fig. 6) illustrate the structure of the succession and spatial relationships of the individual eruptive units. Characteristic lithologies and textures are shown in Fig. 7. Below, we characterize the eruptive units in an upward succession.

5.2. Lower Basalts

The Lower Basalts (**LB**) outcrop mainly along the walls of the lower quarry level (Fig. 6). The observed thickness of the Lower Basalts is 20–30 m. Coherent basalts represent the dominant lithology. They are massive to vesicular, with the vesicles partly filled by zeolites and smectite (August et al., 1995, and references therein), especially in the western and central parts of the quarry. Joints in coherent basalts vary from irregular to platy and columnar. Along the top and margins of the quarry, the coherent basalt grades into irregular zones of basaltic breccias, up to 2–3 m thick (Fig. 7a) and locally into zones of welded scoriae (Fig. 7b). The basaltic breccias comprise densely packed, variably cracked, massive to vesicular (scoriaceous) basalt blocks and variable amounts of finer-grained, altered matrix. Vesicular scoria zones show indistinct boundaries and are characterized by flattened, variably aligned scoriaceous clasts.

The Lower Basalts are overlain by, and laterally interdigitate with the Scoria Breccias and Lapilli-stones (**SBL** – described below). In the lower level of the quarry, the relationships of these two units are generally intrusive: there are several dikes of coherent Lower Basalts pene-



(caption on next page)

UNCORRECT

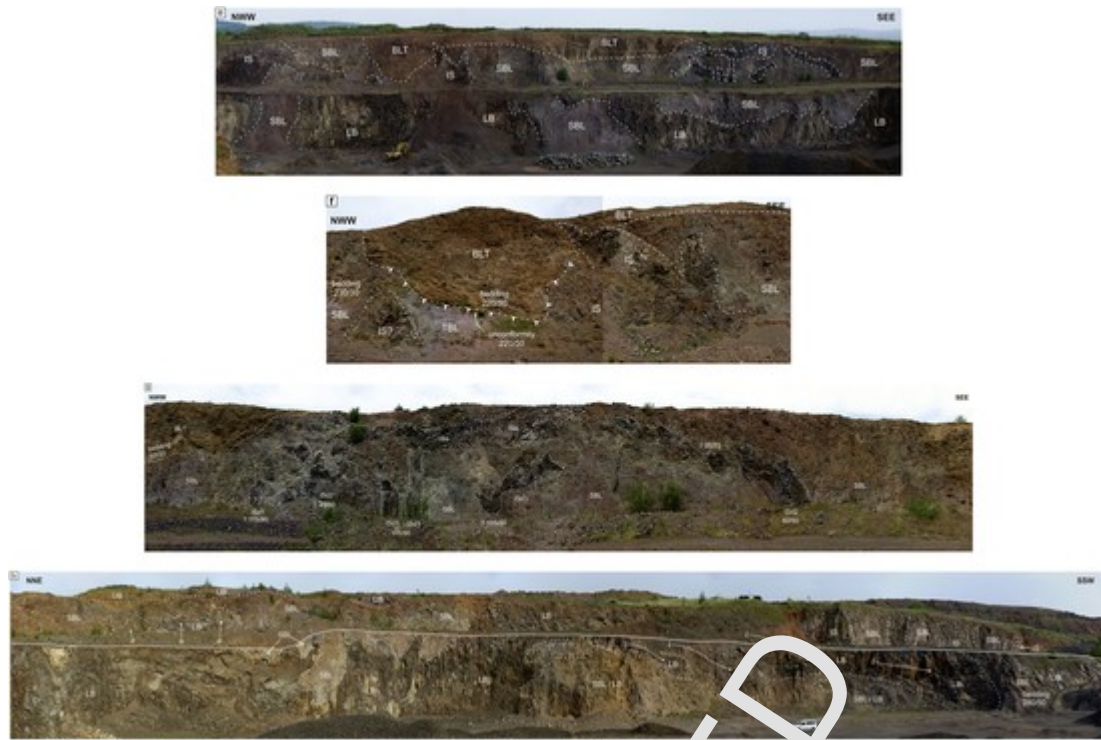


Fig. 6. Annotated photographs of field relationships observed in the Targowica Quarry.

Annotated panoramas of Targowica quarry walls showing spatial relationships of the eruptive units (cf. Fig. 6). Location of sections are shown in Fig. 3. The panoramas start in the south and go clockwise. LB – Lower Basalts, SBL – Scoria Breccias and Lapillistones, WA – Agglutinates, BLT – Bedded Lapilli Tuffs, UB – Upper Basalts, IS – Intrusive Sheets. **6A.** Southern part of quarry. Intrusive contact of Lower Basalts with Scoria Breccias and Lapillistones. Agglutinates above in distance. **6B.** Fault zone in western part of quarry. The SE limb is downthrown by ~20 m to the SW, as suggested by stratigraphic relations and striation rake on the fault plane. The unconformity below the downthrown Upper Basalts is interpreted as inner crater wall contact. An intrusive contact between a sill-like offshoot and the Lower Basalts with overlying Scoria Breccias and Lapillistones. **6C.** Western part of quarry. Scoria Breccias and Lapillistones, strongly altered in this part of quarry, overlain by Upper Basalts. An Intrusive Sheet with subvertical to steeply inclined platy joints is exposed in the north part of section shown. **6D.** Northern termination of the intrusive sheet from (c) comprises finger-like veins in the Scoria Breccias and Lapillistones. Subvertical platy joints, parallel to the margin of this intrusion, are seen in the left. **6E.** Extensive panorama of the north-eastern part of the quarry. This section shows interfingering of Lower Basalts with Scoria Breccias and Lapillistones in the lower quarry level. In the upper level, the Scoria Breccias and Lapillistones are penetrated by Intrusive Sheets (some possibly rooted in the Lower Basalts). The Scoria Breccias and Lapillistones are overlain by the Bedded Lapilli Tuffs, with an unconformity interpreted as a preserved section of inner crater wall in the western part. In addition, this unconformity is transacted by one of the Intrusive Sheets (a dike). Compare details in (f) and (g). **6F.** Bedded Lapilli Tuffs unconformably overlying the Scoria Breccias and Lapillistones, and a dike (one of the Intrusive Sheets) cross cutting the unconformity. **6G.** Numerous Intrusive Sheets in the Scoria Breccias and Lapillistones. Cross-cutting relationships and variable orientations help to distinguish older dikes (ISd1) and younger dikes (ISds) with associated sill (ISs). **6H.** Extensive panorama of the eastern part of the quarry. In the north half of the photo the Lower Basalts in the lower quarry level interfinger intrusively with the Scoria Breccias and Lapillistones; the top surface of the Lower Basalt forms elevations (white arrows “e”) interpreted as tumuli or pressure ridges (see text). However, in the south half of the panorama, the Lower Basalts grade upwards and southwards into lava lobes (white arrows “l”). On top of the sequence the Scoria Breccias and Lapillistones are overlain by a discontinuous cover of the Upper Basalts.

trating into the overlying SBL, and also surrounding rafts of SBL (Fig. 6a). The dikes are platy-jointed parallel to contacts. However, in the eastern part of the quarry and up-sequence, the Lower Basalts grade into extrusive lava lobes interstratified in the SBL; the relationships are “transgressive” in that the lava lobes higher in the succession occur farther along in a southward extent (Fig. 6h). One of better-exposed lava lobes, ~10 m thick and 50–60 m long (Fig. 6h, lower right), shows a coherent interior with columnar joints, fan-like arrangement of the columns at a flow front, and an envelope of basaltic breccia. Other, smaller lobes nearby show a concentric to irregular internal structure.

The top surface of the Lower Basalt flows show relief with local elevations of 5–10 m in amplitude. The surface relief is exposed at the upper eastern (Fig. 6h, upper left) and western parts of the quarry (Fig. 6b, center upper part). At these localities, the massive coherent basalts grade into and is interdigitate with: 1) breccias of vesicular basalts (Fig. 7c), and 2) concentric-structured vesicular basalts (Fig. 7d). The breccias are coarse grained, with a clast-supported closed framework, and comprise relatively large (dm in size), subangular to subrounded blocks of vesicular to spongy basalts with small amounts of

finer-grained matrix. The concentric-structured vesicular basalts form accumulations of tightly-spaced, oval to flattened lava domains, 20–70 cm in larger dimension. Their concentric structure in cross-section is defined by an outer layer of a glassy, massive to vesicular basalt, 5–10 cm thick, surrounding a spongy, strongly altered interior. The complex spatial relationship of the LB and the SBL indicate that the

two units are broadly coeval and formed during contemporaneous explosive and effusive activity of the volcanic system that spanned several eruptive episodes. The thickness of the LB (compared to common basalt flows, typically less than few metres thick) suggest that the LB originated as a ponded lava, possibly a lava lake filling a crater or other topographic depression. During successive episodes of activity this lava lake inflated and resulted in the formation of: 1) dike emplacement in adjacent volcanoclastic deposits in the marginal/lower parts, and 2) lava lobes overflowing the depression/crater rim and the SBL in the upper part. The dikes and the transgressive arrangement of the lava lobes are interpreted to reflect the growth of the volcanic pile with time. The basaltic breccias associated with the coherent basalts include autoclastic breccias and, where present, document the emplacement of aa-type



(caption on next page)

UNCORRECTED



Fig. 7. Annotated photographs of volcanic deposit lithofacies.

Lithofacies in the Lower Basalts (a-d), in the Scoria Breccias and Lapillistones (e-h), the Agglutinates (a-c) and the Upper Basalts (d) and in the Bedded Lapilli Tuffs (m-p). **a.** Massive basalts (mb) grading into basaltic breccias (bb); hammer for scale. **b.** Welded scoria zone associated with coherent basalts; coin is 12 mm in size. **c.** Upper part of a protrusion (outlined; p) on top of Lower Basalts surrounded by breccias of vesicular basalts (br). Field of view c. 2 m wide. **d.** Concentric-structured vesicular basalts. **e.** Massive tuff breccias with abundant volcanic bombs, the largest on left c. 50 cm in length. Several bombs have strongly altered outer shell and appear white on the surface. **f.** Bedded lapillistones. The largest volcanic bomb in photo centre is 20 cm long. **g.** Interstratified tuff breccias and lapillistones with an impact sag around 1 m long volcanic bomb. **h.** Weathered horizon (red) of top of massive tuff breccia; the overlying deposit is the basal part of Agglutinate. **i.** Agglutinates overlying Scoria Breccias and Lapillistones. Arrows point to the palaeosoil horizon on top of the lower of these two units (see close-up in Fig. 7h). **j.** Welded scoria and bombs in lower part of the Agglutinates, c. 2–3 m above the base. Streaks of white-colored post-magmatic minerals accentuate planar fabric. **k.** The upper part of the Welded Agglomerates with flattened bombs, lava slabs (2–3 m long) and discontinuous partings defining the welding foliation of this deposit. **l.** Upper Basalts, densely jointed, overlying Lower Basalts, more altered and locally brecciated, in the entrance trench in southern part of Targowica Quarry. Agglutinates visible at distance in upper left. **m.** Eastern part of the Bedded Lapilli Tuffs outcrop with delineated boundaries of lithofacies a, b, c; see text. **n.** Close-up of the upper part of the Bedded Lapilli Tuffs showing the lithofacies A-C and their depositional structures (see text). **o, p.** Close-up of samples of the Bedded Lapilli Tuffs lithofacies A (coarsely-bedded closed framework lapilli tuffs) and B (medium-bedded open framework lapilli tuffs), respectively, showing their characteristic textures and components (details in text).

lava flows. However, parts of LB lack autoclastic breccias and are likely pahoehoe-type lava flows. Associations of different lava types, often transitional between aa and pahoehoe “end members” are common in modern lava fields (Rowland and Walker, 1987, 1990). In addition, the occurrence of welded scoria can be linked to local spattering, e.g. at the margins of the inferred lava lake, or from hornitoes on top of the lava flows.

At the top of the Lower Basalts along the upper levels of the quarry there are locally irregularities resembling, in simplest interpretation, small apophyses or finger-like intrusions. These are, however, only associated with specific lithologies which point to a more complex origin of these features. The elevations of the top of the LB can be linked to the inflation process and is interpreted as tumuli, or pressure ridges; yet their oval or linear geometry, despite good exposure, is not well determined. Tumuli on modern lava flows are often fractured and associated with collapse-type breccias, protrusion spines as well as squeeze-up lavas (e.g. short toothpaste or pahoehoe lavas, examples in Applegarth et al., 2010, and references therein). Several features of these types can be identified at Targowica quarry. In particular, the relatively narrow, steep to subvertical irregularities on top of the LB can be identified as protrusions, whereas breccias of vesicular basalts (lithologically / texturally distinct from other autoclastic breccias and from pyroclastic rocks of the SBL unit) are interpreted to have formed during breaking and collapse of the solidified protrusions, or the crust of tumuli, and local piling of resulting blocks. The concentric-structured vesicular basalts can be interpreted as compound pahoehoe type flows (pahoehoe toes) squeezed-up from the interior onto the surface of main lava flow, or into open fractures in earlier-solidified lava. The concentric-structured vesicular basalts, however, also resemble pillow lavas; especially in their overall geometric form. The formation of pillow lavas would require the emplacement of the lava flow into a water body, or an underwater eruption. We envision an ephemeral lake that formed during the emplacement of the LB (e.g. due to accumulation of water inside a crater, or due to damming of a river valley by the volcanic deposits). In this case, however, the formation of the lavas as pillows in underwater environment seems less likely because: 1) there is no other evidence for a standing water body (e.g. in the form of some alluvial or lacustrine sediments), 2) the concentric-structured lavas are not associated with depressions but with elevations of LB top, 3) unlike pillow lavas and/or associated hyaloclastites, the concentric-structured lavas and associated breccias are highly vesicular to spongy; this argues against contact with water which results in the inhibition of vesiculation, and 4) the similarity to pillow lavas is rather superficial, as pillows typically show significant radial arrangement of fracture (apart from concentric, e.g. McPhie et al., 1993) which is lacking.

5.3. Scoria Breccias and Lapillistones

The Scoria Breccias and Lapillistones (**SBL**) are exposed along most walls of the quarry and comprise the most widely distributed eruptive unit at the Targowica quarry (Fig. 6). Laterally continuous and the thickest accumulations, up to 20–30 m, occur in the northern and eastern parts of the quarry. The thinnest deposits of a few meters are only found in the westernmost end of the quarry. These deposits are variable in terms of depositional structures, textural characteristics, types of dominant clasts, and the degree of post-magmatic alteration. Two main lithofacies can be distinguished: 1) scoria breccias (Fig. 7e), and 2) lapilli-stones (Fig. 7f). The scoria breccias represent the dominant lithofacies. These deposits are usually non-bedded to poorly bedded, poorly sorted and comprise lapilli-sized scoria with variable amounts of basaltic bombs and blocks. In places, spindle-shaped bombs as well as spatter are more abundant and the deposit grades into agglomerates (sensu McPhie et al., 1993; Le Maitre et al., 2002; equivalent to tuff-breccia sensu Fisher, 1966). Post-magmatic alteration is moderate to strong, especially in the western part of the quarry, and the color of the

deposit varies from grey in less altered to yellowish, red brown and purple in the most altered deposits. Pinkish smectite often fills pore spaces as a cement (cf. Kościówko et al., 1986; August et al., 1995). The lapilli-stone lithofacies are less widespread and found locally on top of the scoria breccias in the W, NE and SE. In the latter area, the lapilli-stones are up to ~6 m thick and bedded. Bedding is partly diffuse and laterally discontinuous, the beds are a few dm thick and comprise relatively well-sorted, alternating layers of fine and coarse scoriaceous lapilli deposit, with sparse bombs and blocks. In the eastern part of quarry, interstratified scoria breccias and lapilli-stones are exposed (Fig. 7f, g). An impact sag associated with an ~1 m long spindle-shaped bomb suggest a ballistic fall from a northern to north-eastern directions. A characteristic red-brown horizon, up to 20 cm thick, is developed in the uppermost part of the described unit, on top of the scoria breccias. It can be traced over a lateral distance of up to ~20 m in the northern part of the quarry, underneath the Bedded Lapilli Tuffs, and for a few metres in the southern part underneath the Agglutinates, where it is best accessible (Fig. 7h, i). This horizon is distinguished by abundant red-brown matrix (clay minerals stained with Fe-oxides/hydroxides) with dispersed, variably altered scoria and volcanic bombs.

We interpret the Scoria Breccias and Lapilli-stones as a pyroclastic fall deposits which can be linked to Strombolian-type eruptions (cf. Awdankiewicz, 2005). The main features of the scoria breccia lithofacies, such as thick, rather massive beds, poor sorting, abundance of volcanic bombs, suggest relatively rapid, near-vent deposition due to the accumulation of predominantly ballistic clasts. The lapilli-stones are well-bedded with a high degree of sorting, and finer-grained. They can be linked to the pyroclastic fall from an eruption column at some distance from the vent. The distribution of the deposits, with a general thickening to the north and north-east, together with ballistic fall direction inferred from a single impact sag, suggests that the vent system is located N-NE of the present quarry. The red-brown horizon on the top of the unit is interpreted as a weathered horizon / initial palaeosol, locally (in the southern part of the quarry) thermally overprinted by the heat from overlying agglutinates. Such horizon suggests that a relatively long repose period, long enough for enhanced weathering, followed the eruption and accumulation of Scoria Breccias and Lapillistones.

5.4. Bedded Lapilli Tuffs

The Bedded Lapilli Tuffs (BLT) are exposed in the northern part of the quarry only (Fig. 6e, f). Their lateral extent is ~100 m and up to 10 m in thickness. Compared to other eruptive units, the Bedded Lapilli Tuffs are distinguished by well developed bedding as well as a yellow-brown color likely due to intense alteration. Three lithofacies can be distinguished (Fig. 7m-p): A) coarsely-bedded closed framework lapilli tuffs, B) medium-bedded open framework lapilli tuffs, and C) coherent lava. Lithofacies A and B dominate the exposures and are interstratified 1 m - 4 m thick units. Lithofacies C forms a single, thin intercalation in the upper part of the sequence. Overall, lithosomes of B show a stratiform to lensoidal geometry and the lenses wedge out to the east-south-east. Bedding shows a variable orientation, partly due to the lensoidal internal lithofacies architecture, and partly due to deposition upon a palaeosurface with significant volcanic relief (Fig. 6f, 7n). Lithofacies A is characterized by relatively poor bedding compared to B. The bedding planes are laterally discontinuous and locally indistinct, and are spaced at distances of several tens of centimetres. The deposit is, however, relatively well-sorted with a matrix supported closed framework. The clasts, typically in the fine-lapilli fraction (usually < c. 2 cm), comprise angular, microvesicular scoria as well as relatively massive, angular basalt fragments. In places there are larger basaltic bombs and blocks. There is an abundant yellowish to orange-colored smectite cement (cf. Kościówko et al., 1986; August et al., 1995). Lithofacies B shows well developed planar, locally wavy to low-angle cross-bedding (best devel-

oped in the upper, inaccessible upper parts of the quarry wall). The beds are from a few to 20–30 cm thick. Compared to lithofacies A, sorting is poor and the clasts range from ash fraction to larger blocks up to ~0.5 m in size with larger clasts dispersed in the finer matrix. The lapilli- and block-sized clasts are angular and relatively heterogeneous, comprising massive to microporous as well as spongy basalts which are variably altered and black, grey, brown or red in color. Lithofacies C is a coherent basaltic lava 30 cm thick and > 10 m in lateral extent. The adjacent volcanoclastic deposits are reddened along a 10–15 cm thick basal contact zone and a similar, but less distinct coloration occurs also along the top contact. The basalt is massive to vesicular and in the central part there are larger, flat cavities, up to 15 cm long.

The depositional structures, textures, and lithological features indicate that lithofacies A was deposited as a pyroclastic fall and lithofacies B by a pyroclastic surge. Overall, these deposits can be interpreted as products of a phreatomagmatic eruption. Lithofacies A, however, bears some features of Strombolian fall deposits (e.g., larger abundance of scoria clast and rare volcanic bombs). Lithofacies B shows features more typical of phreatomagmatic deposits (e.g., abundant, angular, heterogeneous lithic clasts). Possibly, the eruption oscillated between a mixed, phreatomagmatic/Strombolian style and more pronounced phreatomagmatic style, and this resulted in alternating episodes of fall and surge deposition and some variation in lithology of deposits. The lack of non-volcanic country rock fragments in these deposits suggest that magma-water interaction occurred at a shallow level. Specifically, within the older deposits of the Sośnica volcano were the underlying volcanic material was partly incorporated into the phreatomagmatic eruptive products as variably altered, heterogeneous basaltic clasts. In addition, the minor, although distinctive lithofacies C, represents a thin pahoehoe-type lava flow that reflects a lava effusion in later stages of the eruption. The reddening of the surge deposits overlying the pahoehoe lava flow likely indicates the deposition of surge material upon a still hot lava flow surface evidencing a rapid succession of eruptive events.

The bedded lapilli tuffs overlie a paleosol developed on top of the underlying Strombolian eruptive unit. Thus, the phreatomagmatic eruption of bedded lapilli tuffs occurred after a quiescence period long enough for surface weathering of the older deposits to occur, as well as shallow hydrothermal alteration, and accumulation of groundwater in the subsurface. These various factors facilitated: 1) phreatomagmatic eruption when activity resumed, and 2) incorporation of heterogeneous, variably altered, older volcanic material in the erupted tephra. The variable dips of bedding and relation to underlying eruptive units suggests that the bedded lapilli tuffs in the exposed section overlie a topographic crest of the paleo-crater associated with the underlying Strombolian unit. It is inferred that in the NW part the Bedded Lapilli Tuffs overlie SW-dipping inner crater wall (Fig. 6f), whereas in the SE part it was deposited on the northerly to easterly dipping outer slope of the cone. The lensoidal form of facies B lithosomes may reflect transport directions in the pyroclastic surges directed to the west, and thus an eruption vent to the east.

5.5. Agglutinates

The Agglutinates (WA) are exposed in the SW part of the quarry (Fig. 6a, b). Their lateral extent is ~400 m with a thickness up to 15 m in the central part, decreasing to a few meters to the northwest and south, especially across a NE-SW trending fault or a system of such faults. Within the thickest section (Fig. 7i), the lower part (Fig. 7j) comprises partly welded scoria and basaltic bombs up to 30 cm in size with an upward increase in clast size and degree of welding (Fig. 7k). In the upper most part, highly flattened bombs occur up to 3 m – 5 m long that grade into elongated lava shreds, the largest observed being c. 1 m thick and 10 m in lateral extent. These elongated lava shreds (observed on the inaccessible part of the quarry wall) are possibly lava flows.

Overall, the deposit shows a diffuse stratification defined by: 1) alignment of flattened clasts (<pebble to cobble sized scoria clasts, spindle-shaped bombs, lava shreds), partly accentuated by streaks of post-magmatic minerals in the lower part, and 2) discontinuous partings spaced at distances of tens of centimetres in the upper part. The stratification dips shallow at ~15° degrees to the S and W; but locally to the NE.

The lithological characteristic of this unit indicate rapid deposition and welding of hot tephra, associated with a fall from lava fountaining during weakly explosive, Hawaiian-type eruptions. The upward increase of clast size and degree of welding suggest increasing eruption and accumulation rates during this episode of activity and also a decreasing content of volcanic gasses in the erupting magma. The extensive lava slabs in the upper part, especially the longest ones, may be rootless, clastogenic flows originated due to locally much higher accumulation rate of spatter, e.g. from jets of spatter. In contrast, the partings in the deposit could have formed at localized sites of lower deposition rate, where longer surface exposure of accumulated tephra facilitated cooling and partial solidification. The shallow dip angles of stratification reflect a low repose angle of deforming, hot and plastic tephra. The localized outcrop occurrences only in the southern part of Targowica quarry are interpreted to possibly reflect a southerly directed, inclined Hawaiian lava fountain. The NE-trending fault(s) seem to be a late-syndepositional / late-syneruptive feature. It is inferred that during the Hawaiian eruption of the volcano, the pile of welding, hot tephra became unstable and gradually collapsed to the south / south-east, as indicated by displacement of characteristic horizons across the fault(s) and striations on the fault plane. Few smaller faults of similar orientation (forming a stair and step-like system) occur in the upper part of the collapsed block, but cannot be easily traced in this relatively homogeneous deposit. Displacement due to slumping is also supported by variable dip directions in this deposit. The Upper Basalts that cap the Agglutinates are involved in the faulting. This may indicate the emplacement of the Upper Basalts immediately after the Agglutinates during the same eruption.

5.6. Upper Basalts

The Upper Basalts (**UB**) are found as discontinuous, isolated flows in the west, east and south parts of the quarry (Fig. 6b, c, h). In the west and east, the largest flows are up to 3 m - 5 m thick, 20 m - 30 m in lateral extent with U-shaped bases and flat tops. In addition, their are associated thinner flows (1 m or less). The basalts are coherent and massive to moderately vesicular. In the basal parts of the flow, the vesicles are flattened and reach from mm to cm long. The basalts show a combination of platy joints parallel to the base and prismatic joints perpendicular to base; breccias are lacking. The intersection of the joints is characterized by blocky, partly irregular disintegration of the rock. In the southern part of the quarry, along the SSW-trending entrance trench, a major basalt flow over 300 m long, ~130 m wide and 30 m thick occurs (Awdankiewicz, 2005). The flow shows well developed platy joints parallel to its base and fan-like columnar joints perpendicular to the base. The variable orientation of the basal plates and internal columns revealed that this basalt formed two subparallel lobes, surrounding a ridge in underlying deposits, and filled a southerly aligned depression with steep eastern and western margins. Locally preserved top breccia indicates an aa-type flow (Awdankiewicz, 2005). Since 2000, the majority of this basalt flow has been excavated during the quarry operations and only small remnants can be discerned along the entrance trench as platy- to prismatic-jointed lava overlying older volcanic deposits (Fig. 7l).

The Upper Basalts comprise a system of lava flows that cap the volcanic succession at Targowica. The observed geometry and internal joints of the smaller flows (3 m – 5 m thick) in the west and east suggest that they filled local, wide and shallow depressions, likely on the outer

slopes of the volcanic cone, with associated thin lava sheets (<1 m thick) covering adjacent areas. A uniform internal structure and the lack of autoclastic breccias indicate simple pahoe-hoe flows. The major flow along the southern entrance trench is interpreted as a thick aa-type flow that filled a major depression and breached the southern flank of the volcanic cone (cf. Awdankiewicz, 2005). As outlined above, the emplacement of the Upper Basalts probably followed the deposition of Agglutinates in a late phase of the same eruption.

5.7. Intrusive Sheets

Intrusive Sheets (IS) of basalt crop out in the northern and eastern sections of the quarry (Fig. 6c-g). These are mostly dikes up to ~4 m wide. The intrusive sheets consist of coherent basalt, massive to moderately vesicular, often with well developed platy joints parallel to the contacts with the country rocks. The intrusive sheets cut the scoria breccias and lapilli-stones (Fig. 6g). One dike cuts the bedded lapilli tuffs (Fig. 6f). In the NW sector of the quarry, some of the intrusive sheets can be traced across quarry levels, into the Lower Basalts, where they are rooted (Fig. 6e, left part). The most complex system of intrusive sheets crops out in the middle part of the quarries' northern wall. The area is characterized by several dikes and a 4 m thick subhorizontal sill-like intrusive sheet (Fig. 6g). Based on cross-cutting relations, the intrusive sheets were emplaced in two or more episodes. The smallest dikes are the oldest and strike to the NE which are cut by thicker younger dike that strike to the NW and are associated with the subhorizontal sill-like intrusive sheet. In other parts of the quarry, the strikes of the intrusive dikes are highly variable.

The intrusive sheets document late stage episodes of subsurface magma emplacement into the volcanic system. Across the quarry, the intrusive sheets show variable orientations and, apart from some local veins systems (e.g. in the northern wall), no consistent pattern is identified. This suggests that at the present structural level, emplacement of the dikes, inclined sheets, and sills were controlled by local factors or structures within the volcanic edifice, without influence of a regional stress field. The concentration of intrusive dikes in the northern and eastern sections of the quarry arguably suggests that the main conduit (s) are located in these regions.

6. Geophysical results

6.1. Magnetic measurements

The geomagnetic field map (Fig. 4A) shows large spatial variations of the geomagnetic field across the area (more than 2000 nT). The magnetic lows map positions with a significant amount of reverse polarity mafic lavas as the volcano was active during the reversed orientation of geomagnetic field (see the Paleomagnetic results in following sections). The reverse polarity thermoremanent magnetization is the cause of magnetic minima. The zones, where the differences of magnetic intensity (ΔT) decrease (roughly) below -300 nT are interpreted as areas with a significant amount of in-situ basalts. In contrast, the magnetic highs (approximately more than 300-400 nT) are interpreted as heaps of basalt gravel - the product of the quarry. Such heaps contain randomly oriented basalt blocks and stones, where the direction of thermoremanent magnetization of individual blocks cancels each other and the overall results are anomalies stemming from induced magnetization only.

6.2. Electrical resistivity tomography

The inverted values of resistivities on individual ERT profiles (Fig. 4B) can be used to differentiate the subsurface lithologies into three groups: (i) the low resistivity zones (resistivities up to approximately 100 Ω m), (ii) the mid-resistivity zones (resistivities approximately be-

tween 100 and 300 Ω m) and (iii) the high resistivity zones (resistivities higher than approximately 300 Ω m). The low resistivity zones could be attributed to clay-rich lithologies (c.f. Tabbagh and Cosenza, 2007; Choo et al., 2016, Hasan et al., 2018). In contrast, the high resistivity areas generally maps the distribution of fresh, coherent basalts (Petronis et al., 2018; Lichoro et al., 2019; Torrese et al., 2021). The mid-resistivities would stand in between these two types as slightly weathered coherent rocks.

7. Paleomagnetic results

7.1. General demagnetization behavior

Twenty sampling sites from individual dikes were collected in the Targowica quarry for paleomagnetic study with 19 sites yielding interpretable results. Of the 19 sites, two sites were of high dispersion and the one other site did not yield stable end-point demagnetization behavior; these three sites are excluded from the group mean calculation (Table 1). We attribute the high dispersion and non-stable end-point behavior of these three sites to either the rocks being lightning struck or chemically altered; these three sites will not be further discussed. We base our interpretation of the Targowica quarry intrusions on the seventeen accepted sites. The majority of the samples were fully demagnetized with a combination of alternating field and thermal demagnetization treatments. Sample magnetizations directions are well-grouped at the site level with most sites yielding a single component magnetization that decays to the origin with less than 10% of the NRM remaining after treatment in an alternating field of up to 120 mT and/or thermal treatment up to 525 °C (Fig. 5). The majority of the samples contain a single characteristic remanent magnetization (ChRM), although some samples contain more than one magnetization component, which is randomized by about 20 mT or 300 °C. We interpret these magnetizations as viscous remanent magnetization (VRM) overprints. After the VRM is removed, the remaining magnetization is likely a primary thermoremanent magnetization (TRM); which we interpret as the ChRM. Paleomagnetic results from seventeen sites yield a total group mean of $D = 206.9^\circ$, $I = -80.4^\circ$, $\alpha_{95} = 11.9^\circ$, $k = 10.0$ ($N = 17$, reverse polarity sites; Fig. 8) The group mean result is statistically indistinguishable to the average mid-Miocene expected field direction based on three poles located geographically near and temporally close in age of the intrusions $D = 205.3^\circ$, $I = -76.4^\circ$, $\alpha_{95} = 4.5^\circ$, $k = 766.4$, $N = 3$ (Table 3) with an inferred rotation of $1.6^\circ \pm 12.2^\circ$ and flattening of $-4.0^\circ \pm 9.7^\circ$ (Beck Jr., 1980; Demarest, 1983).

To test the dispersion of the site mean virtual geomagnetic poles (VGPs), we compared the average VGP dispersion to the predicated dispersion value for the latitude of the site (50.6° N) (Merrill and McElhinny, 1983). If secular variation has been adequately sampled, the observed angular dispersion estimate of site mean VGPs should be consistent with that predicted. The expected dispersion of the VGPs for the latitude of Targowica quarry during the mid Miocene ranges from 18.8° to 16.2° (average = $17.5^\circ \pm 1.3^\circ$) (Table 1; Merrill and McElhinny, 1983). The estimated dispersion (S) of the seventeen accepted site mean directions yields a total group mean VGP dispersion of $38.0^\circ \pm 11.9^\circ$ (95% confidence); a value which is statistically greater than the predicted VGP dispersion estimate. Inspection of the paleomagnetic data dispersion, however, reveals that the majority of sites ($N = 11$) plot more shallow and to the west of the expected mean direction at $D = 196.6^\circ$, $I = -68.8^\circ$, $\alpha_{95} = 4.7^\circ$, $k = 87.2$, $N = 11$. The sub-group site mean data are tightly clustered and plot within 15° of the new group mean direction that is discordant to the expected field direction. The sub-group site mean discordant direction yields a rotation (R) $-8.7^\circ \pm 11.6^\circ$ and flattening (F) $7.6^\circ \pm 4.5^\circ$ relative to the expected field direction (Fig. 8). The remaining six sites show a high degree of scatter (Fig. 8). The estimated dispersion (S) of the eleven site mean directions yields a new group mean VGP dispersion of $13.1^\circ \pm$

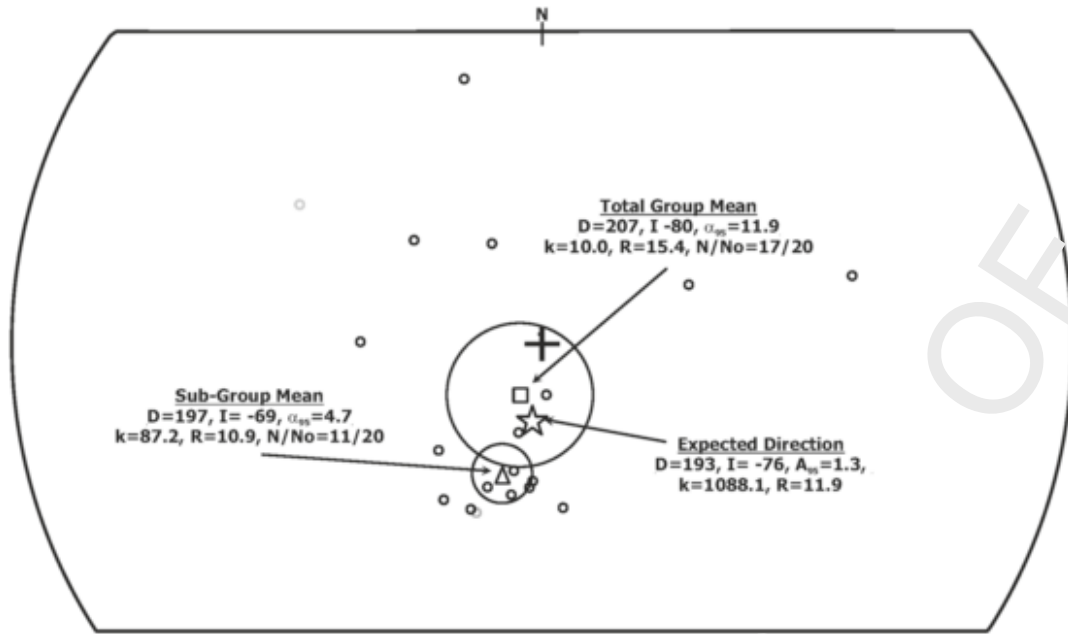


Fig. 8. Paleomagnetic data from the Targowica Quarry.

Group mean paleomagnetic results from the intrusions (black circles are site means ($N = 17$) and the black square with confidence ellipse is the group mean). The site means as grey circles were not included in the group mean calculation as they were of high dispersion (see Table 1). The black star is the expected field direction based on the average published paleomagnetic poles (see Table 3). **Explanation:** Group/Expected mean D° , declination; I° , inclination; α_{95} , 95% confidence ellipse about the mean, assuming a circular distribution; A_{95} , 95% confidence ellipse about the expected field direction; k , best estimate of Fisher precision parameter; R , resultant vector length, N/No , ratio of number of samples used to the number of samples collected.

Table 3

Select paleomagnetic poles for Europe and corresponding expected directions.

Rock Name	Age (Ma)	VGP Position		A_{95}	Expected Direction		(estimated)		Reference
		λ (N°)	φ (E°)		Dec	Inc	A_{95}	k	
[§] Rheinlan Pflaz Volcanics	22.5	70.0	108.0	4.2	19.1		79.0	4.2	[□] Besse and Courtillot (2002)
[§] Lausitz Volcanics	22.5	74.6	120.5	4.5	33.6		75.2	4.5	"
[§] Tertiary Volcanics, northern Bavaria	28.5	78.0	140.0	4.0	21.6		74.9	4.0	"
Reverse Polarity Expected Direction				N	R	Dec	Inc	A_{95}	k
Hocheifel Tertiary Volcanics	34.0	80.8	182.0	2.3	4.8		-76.4	4.5	[□] Besse and Courtillot (2002)
10 Myr sliding window for every 5 Myr									
20	19.6	81.4	149.7	4.5	14.2		76.0	4.5	[#] Besse and Courtillot (2002)
25	26.0	83.8	153.2	5.3	10.3		77.0	5.3	"
30	30.2	81.6	183.4	5.3	4.2		75.0	5.3	"
35	33.7	81.2	173.4	4.6	7.4		75.0	4.6	"
40	39.0	78.8	160.2	7.3	13.6		74.1	7.3	"
20 Myr sliding window for every 10 Myr									
20	18.9	84.0	154.8	2.7	9.6		77.0	2.7	"
30	29.5	82.8	158.1	3.8	10.3		76.3	3.8	"
40	40	81.3	162.4	3.3	10.7		75.4	3.3	"

Age (Ma), age range or age of the paleomagnetic pole; λ (N°) and φ (E°) are latitude and longitude of the paleomagnetic reference pole; A_{95} is the semi-angle of the cone of 95% confidence about the pole; k is the best estimate of the precision parameter of the pole (Fisher, 1953); Expected Direction - Dec, declination, Inc, inclination are expected declination and inclination of the reference directions as calculated for the latitude and longitude of the Targowica quarry, Lower Silesia, SW Poland (16.96°E, 50.69°N); A_{95} is the estimated semi-angle of the cone of 95% confidence about the reference direction; [◆] Selected Paleomagnetic Data for Europe Extracted From the GPMD V3.3 Database; [#] Synthetic Apparent Polar Wander Path; [&] Master Apparent Polar Wander Path; [§] Paleomagnetic poles averaged to calculate a mean pole for the Targowica quarry.

[◆] Selected Paleomagnetic Data for Europe Extracted From the GPMD V3.3 Database

[#] Synthetic Apparent Polar Wander Path

[&] Master Apparent Polar Wander Path

[§] Paleomagnetic poles averaged to calculate a mean pole for the Targowica quarry

4.7° (95% confidence); a value which is statistically in agreement with the predicated. The implications of these observations are discussed more fully below. From this analysis, we suggest that the results may reflect either 1) a time interval covering less than the longer periodicities

of secular variation and do not represent a time averaged result or 2) a tectonic deformation associated with magma emplacement and growth of the Targowica volcano. The group of eleven dikes yields very similar directional data while six dikes each yield distinct directions. As we dis-

cuss below, we prefer the latter interpretation of tectonic deformation to explain these data.

8. Anisotropy of magnetic susceptibility

To estimate the magma flow direction, 290 specimens from 32 different sites were measured. Of the 32 sites sampled, 11 sites are from the four dikes in which paired margin data could be obtained in order to estimate an absolute flow vector (Table 2) based on the imbrication of the magnetic foliation plane (K_1 - K_2 plane) (Knight and Walker, 1988). TVQ1 and TVQ5 yield paired magnetic foliation imbrication that suggests a sub-vertical upwards flow. TVQ6's magnetic foliation imbrication pattern is suggestive of sub-horizontal, moderately inclined, northwest flow and TVQ8 shows a sub-vertical downward flow (Fig. 9). The remaining 21 intrusion sites yield 9 sites that have a prolate susceptibility fabric while the remaining 12 sites are oblate (Table 2; Fig. 9). When T is negative, it defines a prolate magnetic susceptibility ellipsoid that can result from stretching and extension during magma emplacement (Khan, 1962). During magmatic flow, the early-formed crystals rotate and undergo relative translations, and they may provide indirect evidence of magmatic flow path based on the orientation of the K_1 magnetic lineation (Hrouda, 1982; Borradaile and Henry, 1997). The nine prolate sites yield 3/8 sites that indicate north-south flow direction, 2/8 sites that yield an east-west flow direction, and 4/8 sites that suggest northwest-southeast magma flow (Table 2; Fig. 9). The mean susceptibility (K_m) ranges from 49.4×10^{-3} SI - 10.2×10^{-3} SI and average mean susceptibility is 23.65×10^{-3} SI. The remaining 12 sites with oblate-shaped ellipsoids yields a range of strike and dip directions that do not define a clear pattern (Table 2 Fig. 9). The average corrected degree of anisotropy (P_j) is 1.013 and the shape parameter indicates both prolate ($N = 9$) and oblate ellipsoid shapes ($N = 23$).

9. Rock magnetic data

9.1. Rock magnetic data results

Rock magnetic data are interpreted to indicate that the remanence and the AMS fabrics are likely carried and defined by a ferromagnetic (*s.l.*) mineral phase of multidomain (MD) to pseudo-single domain (PSD) grain size of a variable titanomagnetite composition, although some differences were observed. Thermomagnetic experiments (Curie points) reveal that a ferromagnetic mineral(s) phase dominates the susceptibility with little contribution from a paramagnetic phase(s) (Richter and van der Pluijm, 1994; Fig. 10A). Some samples show the presence of an Fe-sulfide phase (pyrrhotite) and/or coarse grained titanomaghemite and evidence of high to moderate Ti-titanomagnetite; evidence of titanohematite was not seen in the thermomagnetic data. Most samples are non-reversible indicating probable oxidation of the Fe- Ti oxide or Fe-sulfide phase during heating. A few samples show a well-defined Hopkinson Peak consistent with the presence of a single domain titanomagnetite phase in addition to the PSD and MD phase(s). Following the modified Lowrie-Fuller test (Johnson et al., 1975) the AF decay of normalized NRM, ARM, and SIRM was compared (Dunlop and Özdemir, 1997). When the ARM yields a medium destructive field greater than the SIRM, it indicates a single-domain (SD) to PSD magnetic grain size (TVQ 1B-E, TVQ 3F, TVQ 11E, TVQ 16A-B, TVQ 22B, TVQ 23A, TVQ 25F). When the ARM is less than SIRM, it indicates a MD magnetic grains (TVQ 20B) (Fig. 10B). IRM acquisition curves show a narrow spectrum of responses, ranging from SD magnetite to somewhat higher-coercivity PSD domain magnetite (Fig. 10C). All samples are likely dominated by cubic, titanomagnetite demonstrating steep acquisition reaching saturation by 0.20 T to 0.40 T.

9.2. Hysteresis and first order reversal curve results

Magnetic hysteresis and FORC data were obtained from six samples from Targowica quarry. All samples yield similar hysteresis loops characterized by steep acquisition and reach saturation in an applied field (H) between 0.46 T and 1.33 T with an average applied field of $0.84 \text{ T} \pm 0.33 \text{ T}$; 1σ ; Fig. 11A). The saturation magnetization (M_s) ranges from 35.30 Am^2 to 152.51 Am^2 with an average of $60.00 \text{ Am}^2 \pm 47.18 \text{ Am}^2$; at 1σ ; Fig. 11A). The saturation magnetization values are consistent with a cubic phase of restricted composition likely titanomagnetite and/or titanomaghemite. First-order reversal curve distributions are used for rapidly examining magnetic domain state. The FORC distribution for an SD grain is highly peaked on the $H_u = 0$ axis and the contours are elongated with negligible vertical spread. Small PSD samples have FORC distributions with a distinctive closed-contour structure. The distributions of the larger MD grains display no peak, and lie close or on the Y-axis. Three samples (TVQ1, TVQ10, TVQ16) yield FORC distributions above and below the zero Y-axis and are slightly elongated along the X-axis (Fig. 11B). The remaining three samples (TVQ5, TVQ8, TVQ19) plot close to the Y-axis with minor elongation along the X-axis. Collectively, the six samples show similar results and are consistent with a mixture of domain states; likely SD, PSD, and MD (Fig. 11B).

10. Discussion

The results from the Targowica quarry and surrounding area provide information about the evolution of the Sośnica Hill volcano(s) that can be used to constrain the subsurface geometry, evolution of the magma plumbing system, and surface morphology of the volcano. Previous interpretations of the Targowica quarry envisioned a vertical conduit with many dikes emplaced away from the central feeder system (Awdankiewicz, 2005). Here, we present a revised interpretation that outlines a more complex and time transgressive development of the magmatic system involving multiple magma feeder conduits, several vents, variable eruptive styles, and an evolving geomorphology of the surface landscape around the volcanic constructs.

10.1. Implication of geophysical patterns

Ground geophysical methods provide a useful tool for imaging the internal structure of volcanoes (e.g., Peccerillo et al., 2006; Finizola et al., 2010; Skácelová et al., 2010; Bolós et al., 2012; Blaikie et al., 2012, 2014; Schmidt et al., 2013; Barde-Cabusson et al., 2013; Bolós et al., 2014; Valenta et al., 2014a, 2014b; Flechsig et al., 2015; Marshall et al., 2015). All of the basaltic intrusions were erupted and cooled down below their Curie point during a reversed polarity magnetic field likely between Chron C11 to C7; although the current geochronology resolution does not allow us to refine the magmatism to a specific reverse polarity Chron. Fig. 4A depicts deviations of the geomagnetic field (dT), the values of magnetic intensity are negative; opposite to the orientation of the current geomagnetic field thus the vectors subtract and yield a total value (T) lower than the surrounding rock (e.g. Urrutia-Fucugauchi et al., 2012 or Prezzi et al., 2017). The magnetic low in the north part of the quarry likely reflects the intrusive sheets and Lower Basalt flow (Fig. 4A). The sharp linear boundary of the magnetic low in the NW part of the quarry is attributed to a rapid lithological change caused by the juxtaposition of different rock types related to displacement along the fault zone (Fig. 2A; Fig. 4A). The resistivities of volcanic rocks generally depend on the mineralogical composition, porosity and pore-fluids present in the materials. The high resistivities generally corresponds to unaltered lavas or unaltered volcanoclastics (e.g. Petronis et al., 2018; Lichoro et al., 2019; Rappich et al., 2019; Torrese et al., 2021). In contrast, the low resistivities (in this context) likely correspond to altered, clay-rich lithologies such as weathered scoria and tuff

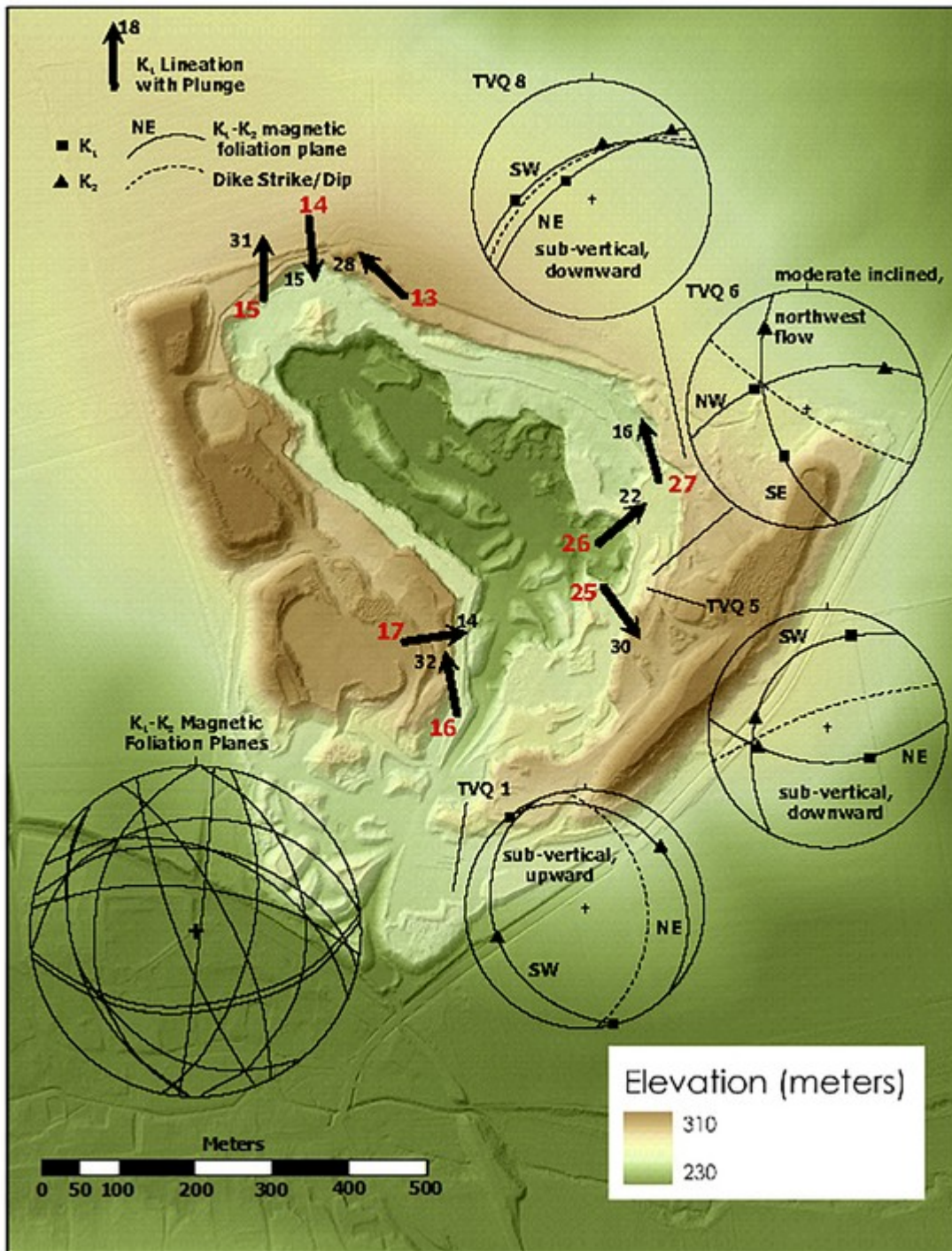
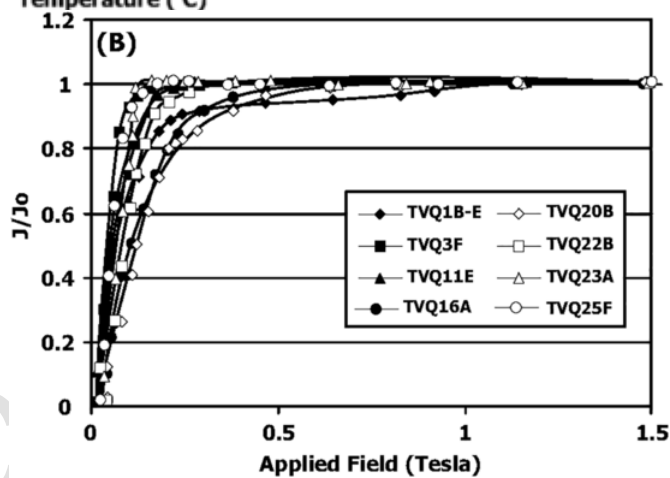
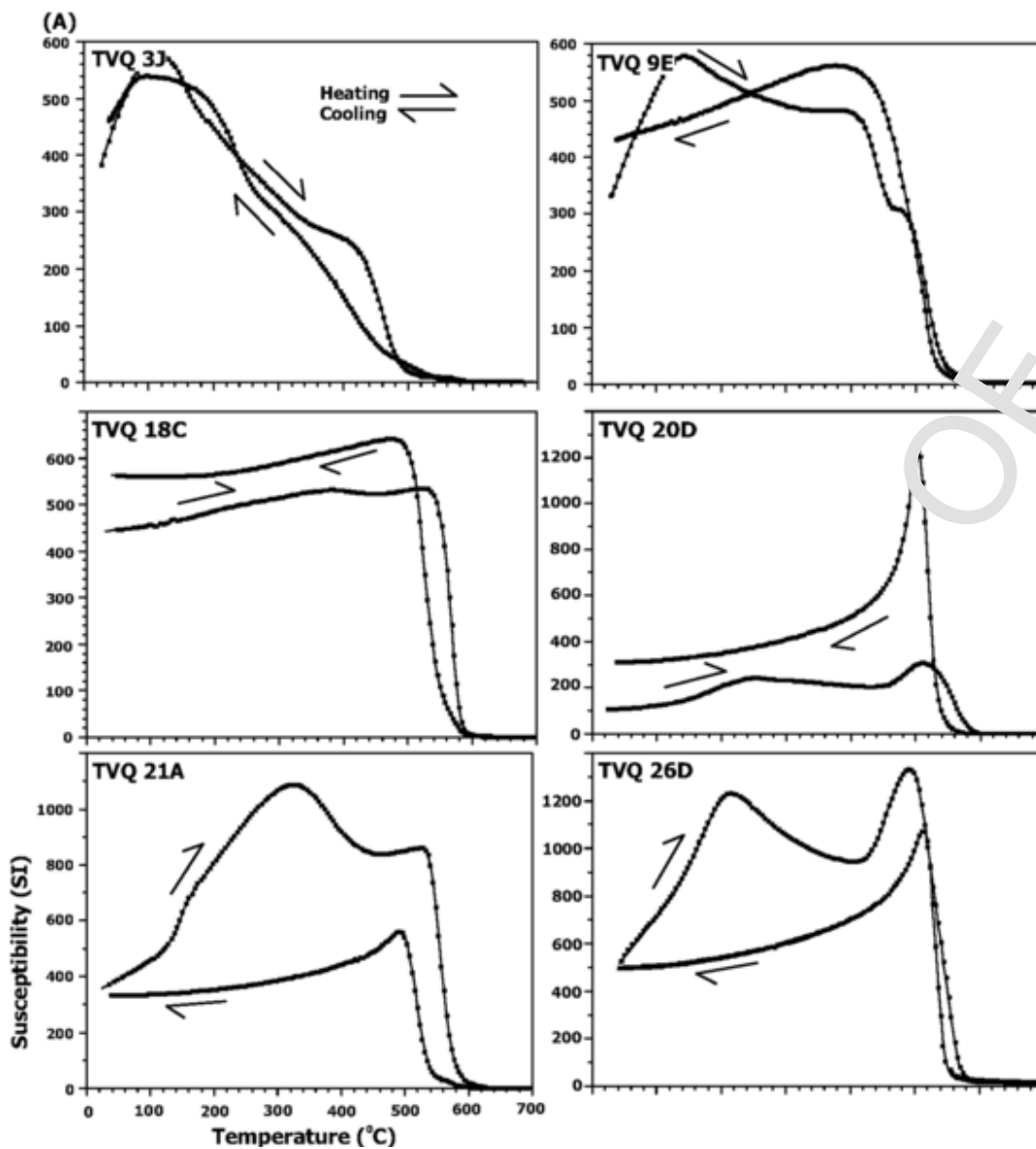


Fig. 9. Anisotropy of magnetic susceptibility data.

Digital elevation model of the Targowica quarry showing the anisotropy of magnetic susceptibility data with inferred magma flow directions. Bottom left stereographic projection is the K_1 - K_2 magnetic foliation plane data from sites that yield an oblate susceptibility ellipsoid. The remaining stereographic projections (TVQ1, TVQ5, TVQ6, TVQ8) are lower hemisphere equal area projection of the K_1 - K_2 magnetic foliation plane from dikes with paired margin data allowing the direction of magma flow to be estimated. Three categories of magma flow are observed (1) subvertical downward flow, (2) subvertical upward flow, and (3) subhorizontal inclined downward flow. Eight other sites (red numbers) yield prolate shaped ellipsoids with K_1 -lineation indicating shallow (32° - 14°) subhorizontal flow; the remaining sites yield oblate shaped ellipsoids with an indeterminate flow direction (Table 2). These data are interpreted to indicate that feeder dikes bring magma from depth into the volcano and a complex network of branching dikes distribute magma away from the vent conduit towards the flanks of the volcano leading to potential side eruptions. (For interpretation of the references to color in this figure legend, the reader is referred to the web version of this article.)

(Ghorbani et al., 2018; Lichoro et al., 2019) or soils and alluvium. The increased level of alteration increases the net amount of clay minerals which decreases the total resistivity (c.f. Tabbagh and Cosenza, 2007; Choo et al., 2016, Hasan et al., 2018). Although there were no resistiv-

ity values measured in the laboratory given the complexity of correlating lab to field values, the lithologies found by geological mapping in the area are assigned to the three resistivity groups reflecting mainly the variable amount of clays. The low resistivity zones are interpreted



(caption on next page)

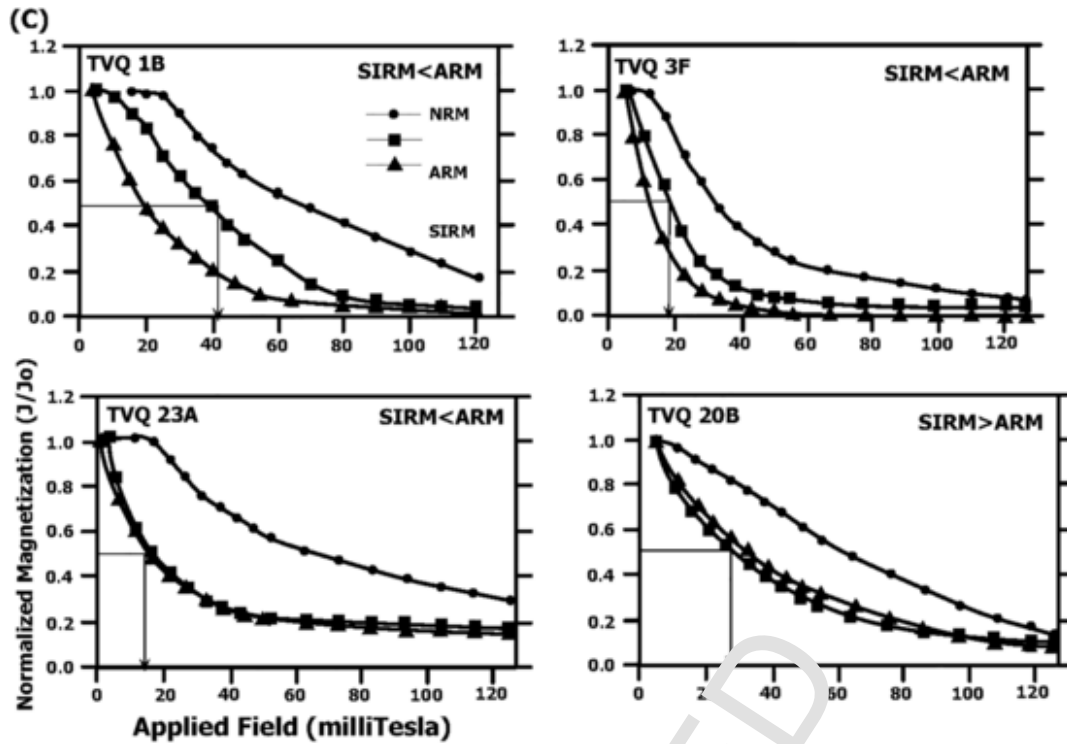


Fig. 10. Rock magnetic experimental results.

10A. Continuous low-field susceptibility versus temperature experiments from representative samples from the Targowica quarry. Results indicate a range of high to low Ti- titanomagnetite compositions and evidence of an Fe-sulfide phase (pyrrhotite). **10B.** Modified Lowrie-Fuller test comparing AF demagnetization response of natural remanent magnetization (NRM), anhysteretic remanent magnetization (ARM), and saturation isothermal magnetization (SIRM). $SIRM < ARM$ = single-domain grain size, $SIRM > ARM$ = multi-domain grain size. **10C:** Normalized acquisition of isothermal remanent magnetization (IRM) from representative samples. The steep acquisition and saturation by between 0.25 T and 0.40 T is indicative of titanomagnetite of a restricted single domain to pseudo single domain grain size. Normalized backfield IRM curves (not shown) yield coercivity of remanence values by -0.04 to -0.07 T; typical of titanomagnetite with a low-Ti composition.

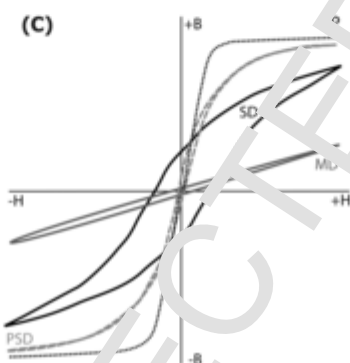
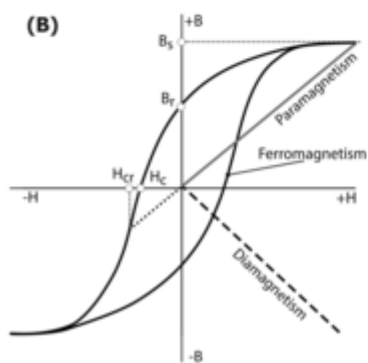
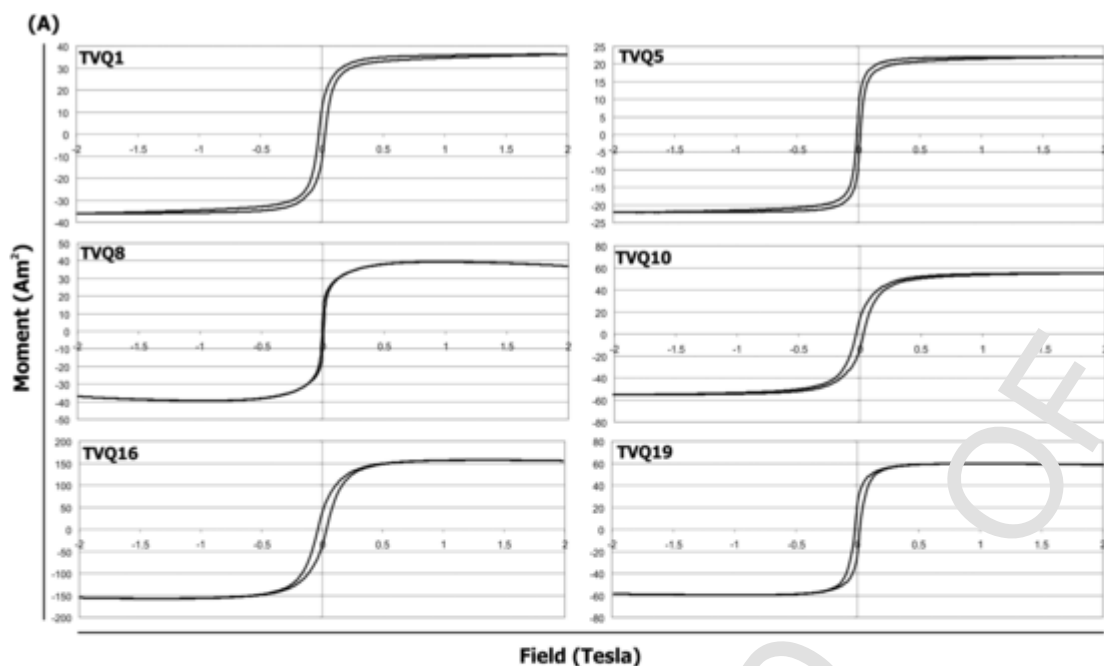
as weathered tuffs and scorias or to the soil and alluvium. The latter is the case of the Profile 1 located outside of the quarry. The mid-resistivities are interpreted as slightly weathered bedrock – i.e., crystalline schists of the Kamieniec Metamorphic Belt (Fig. 2A; Fig. 4B). The high resistivity areas map the distribution of fresh, coherent basalts. The high resistivity on the ERT data (Fig. 4B) are generally interpreted to represent coherent dry rocks with a low clay content likely coherent lava flows and/or dry gravel used to level the quarry floor (e.g., the small near-surface anomalies at the northwest part (0–50 m) of the profile 4; Fig. 4B). In contrast, the low resistivity likely represent rocks or soil containing large amount of ions to conduct electricity such as weathered volcanoclastics and soil rich in clay. Profile 2 crosses the course of three dikes cross cutting the bedrock and visible in the quarry walls (see Table 1, Fig. 4B). The profile 4 shows the fault zone visible on the outcrop and supports the interpretation of the hanging wall on the southeast (a similar pattern observed e.g. Finizola et al. (2006) on the Stromboli volcano).

10.2. Implications of the paleomagnetic data

In this study, paleomagnetic data are used to test whether the Targowica quarry intrusions are tilted and/or rotated in response to deformation associated with the growth of the Sośnica Hill volcano(s). Demagnetization data reveal that 17/20 sites contain a stable, single component reversed polarity magnetization. Eleven sites are well-grouped and the group mean is discordant to the Oligocene expected field direction while six sites are discordant and scattered relative to the other eleven sites and from the Oligocene expected field direction (Fig. 8). The group mean direction from the eleven sites ($D = 196.6^\circ$, $I = -68.8^\circ$, $\alpha_{95} = 4.7^\circ$, $k = 87.2$, 11R) is statistically distinguishable

from a mid-Neogene expected direction ($D = 205.3^\circ$, $I = -76.4^\circ$; $A_{95} = 4.5^\circ$, $k = 766.4$) for southern Poland based on comparison to the average paleomagnetic poles from three units for the region (Table 3; Besse and Courtillot, 2002). The estimated dispersion (S) of the eleven site means ($S = 13.1 \pm 4.7$) is statistically indistinguishable than the predicted model (average = $17.5^\circ \pm 1.3^\circ$). Two possible explanations for the less than predicted dispersion are that 1) the dikes were emplaced quickly relative to secular variation and the data represent a spot reading of the geomagnetic field or 2) uniform tectonic deformation associated with magma emplacement and the growth of the Targowica volcano. We argue here that the eleven sites were emplaced quickly relative to secular variation and have experienced only minor deformation. The other six sites, however, are intrusions that experienced differential subvolcanic deformation involving rotation and tilting following remanence acquisition yielding the scatter of the individual site mean directions.

Based on the paleomagnetic data we envision a scenario of protracted volcanic system evolution with multiple episodes of magma emplacement and associated subvolcanic deformation. The Sośnica Hill volcano formed in five eruption stages over an extended period of time (Table 4). 1) *Initial volcano growth:* Development of the volcano began with magma ascent that cuts through the local bed rock and once reaching the near surface served as a feeder conduit for the first eruption. The first eruption stage produced thick pyroclastic deposits forming a cone (Awdankiewicz, 2005). The main central vent of the cone was located north of the quarry. 2) *Phase 1 dikes emplaced:* In the second stage, more magma was supplied into the vent and lava flows breached the southern flank of the cone and flowed southwards. After the supply of magma was depleted, the eruptions paused until an equilibrium pressure was reached allowing the magma to solidify completely. 3) *Renewed subvol-*



Mineral	X	T_c (°C)	σ_s (Am ² /kg)
Magnetite	Fe ₃ O ₄	575-585	90-92
Hematite	α Fe ₂ O ₃	675	0.4
Maghemite	γ Fe ₂ O ₃	-600	-80
Pyrrhotite	Fe ₇ S ₈	320	-20
Greigite	Fe ₃ S ₄	-333	-25
Goethite	α FeOOH	-120	<1

X - composition, T_c = Curie or Néel Temperature
 σ_s = saturation magnetization

(caption on next page)

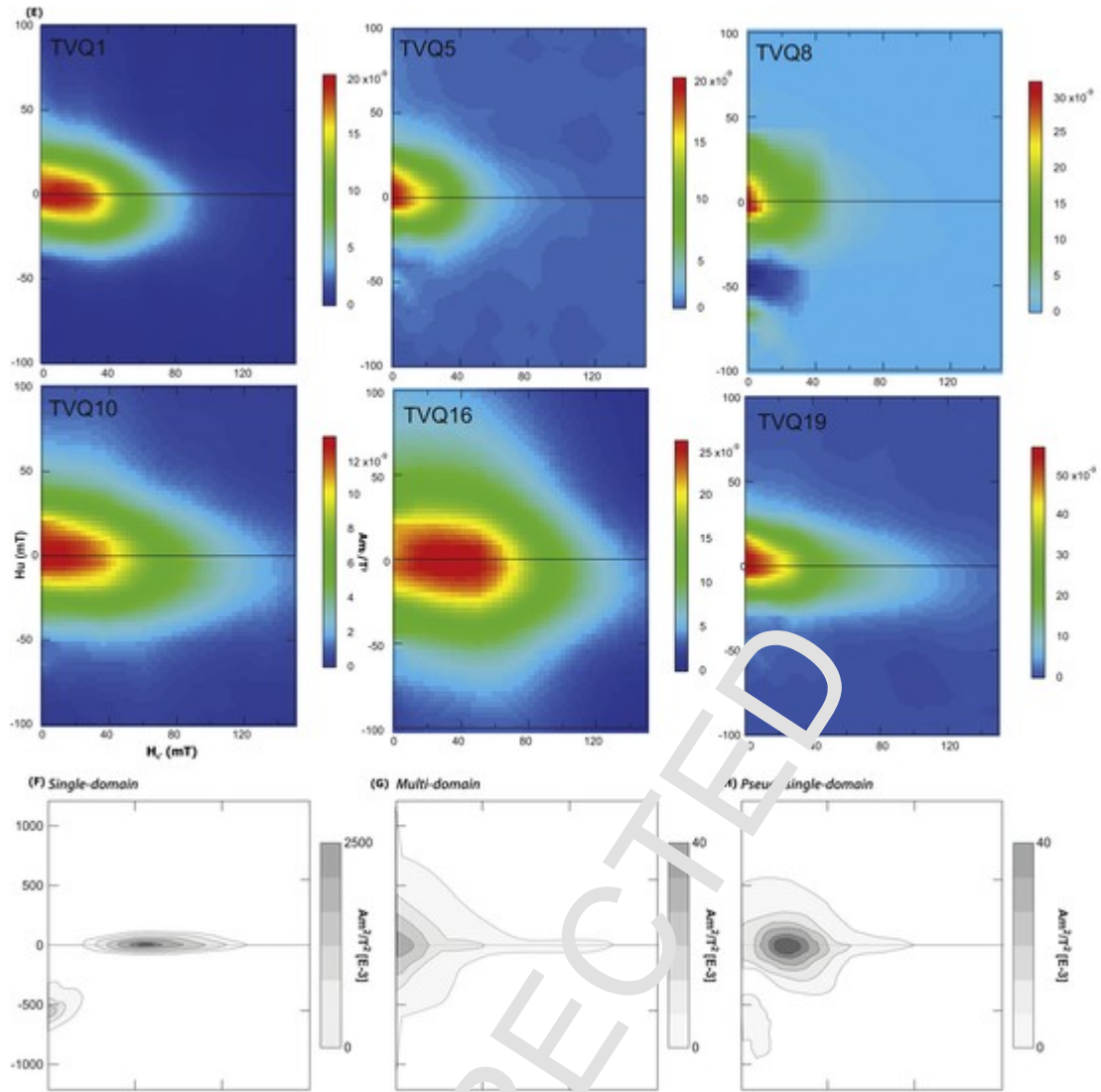


Fig. 11. Representative hysteresis diagrams and first order reversal curve (forc) distributions.

11A-11E: Representative Hysteresis Results and Idealized Hysteresis Curves. **11A:** Representative hysteresis loop diagrams. Magnetic hysteresis parameters (i.e., saturation remanent magnetization, M_s ; saturation magnetization, M_s ; and coercive force and coercivity of remanence, H_c and H_{cr} , respectively). **11B:** Ideal hysteresis curves showing magnetization behavior of diamagnetic, paramagnetic, and ferromagnetic (*s.l.*) materials. B_s , saturation remanent magnetization; B_s , saturation magnetization; H_c , coercive force, H_{cr} ; coercivity of remanence; H , applied field; B (+/-), positive/negative induced magnetization (induction); H (+/-), positive/negative applied magnetic field. **11C:** Ideal hysteresis behavior for a ferromagnetic (*s.l.*) material of different domain states. SP, superparamagnetic; SD, single domain; PSD, pseudosingle domain (vortex state); MD, multidomain. **11D: Inset Table:** Mineral, common ferromagnetic (*s.l.*) and antiferromagnetic mineral phases found in rocks and sediments; X, chemical formula of the mineral; σ_s , saturation magnetization (Am^2/kg) at room-temperature (modified from Dunlop and Özdemir, 1997). **11E:** FORC distributions of samples from the Targowica quarry. H_a , negative saturation applied field; H_b , positive saturation applied field; $H_u = (H_a + H_b)/2$. **11F-11H:** Idealized First Order Reversal Curve (FORC) diagrams for (F) single domain (SD) (G) multidomain (MD), and (H) pseudosingle domain (PSD) for magnetite grains (modified from Harrison et al., 2018). **11F:** The magnetic domain size for stable SD grains is between $\sim 0.03 \mu\text{m}$ to $\sim 0.08 \mu\text{m}$, PSD grains are variable $> 0.1 \mu\text{m}$ to $20 \mu\text{m}$, and MD are $> \sim 20 \mu\text{m}$ (Dunlop, 1973; Dunlop (1995). However, the particle size range over which the transitions occur depends on many factors such as temperature, spontaneous magnetization, shape, and the state of internal stress of a particle (e.g., Day et al., 1977; Dunlop and Özdemir, 1997; Heider et al., 1987). Magnetite grains with different domain structures plot in different parts of the FORC distribution diagram. Single domain grains yield a narrow size-shape distribution with a single peak on the B_c (i.e., $B_u = 0$) axis. **11G:** Multidomain grain sizes show a broad, vertically spread signal along the B_u direction with a weak, high-coercivity, horizontally spread tail perpendicular to the B_c axis (Pike et al., 2001). **11H:** Intermediate grain sizes of the pseudosingle domain size (vortex state; Roberts et al., 2017) yield a well-defined closed-contour peak with a broad vertical and horizontal spreading along both B_c and B_u axis. (B, C, D, F, G, H modified from Žák et al., 2021 in press).

canic magmatic activity: In stage three, the activity resumed on the western side of the main cone, where a small vent and construct probably formed. After the formation of this smaller cone, the activity ceased and erosion of the volcanic edifice ensued. 4) *Final (?) phase of dike emplacement occurs:* Subvolcanic deformation of the “guts” occurs resulting in tilting and rotation phase 1 dikes (Fig. 12; Table 4).

10.3. Anisotropy of magnetic susceptibility data

In order to gain an understanding of magma emplacement, it is important to consider the geometry, magma flow processes, physical controls on emplacement, and the regional deformation pattern at the time of intrusion. In the simplest of circumstances, the rock fabric of crystallized magma preserves either of two end-member processes. The fabric

Table 4

Tabulated evolution of eruptive and subvolcanic processes.

Eruptive unit	Eruptive styles	Surface structures	subvolcanic units, structures and processes	relative age
Upper Basalt	Effusive	Major lava flows in the south through a breach in crater rim		Youngest
Welded Tuff Agglomerate	Hawaiian	Welded tephra accumulations in south	Reorientation of early dikes due to deformation of the volcanic edifice by later batches of intruding magma	
Bedded Lapilli Tuff	Phreatomagmatic	Phreatomagmatic tephra accumulations in the north-northwest	Changing transport directions of magma in dikes (outward, upward / inward, downward)	
Repose period, weathering				
Lower Basalt	Effusive	Lava lake, lava lobes/overflows to south-southeast, locally tumuli, hornitoes	Emplacement of Intrusive Sheets in several episodes associated with eruptive episodes	
Scoria Breccia and Lapillistone	Strombolian	Widespread Strombolian deposits, initial crater(s)		Oldest

Tabulated evolution of eruptive and subvolcanic processes and resulting structures observed and/or inferred at Targowica quarry. The table reads from base upwards.

may reflect a magma flow direction (stretching direction) because elongate minerals are often rotated under simple-shear into the flow-plane defining a flow-lineation (Jeffery, 1922). Alternatively, the magmatic foliation develops in relation to the regional orientation of the maximum principal shortening direction acting at the time of emplacement which preferentially orients most planar crystals normal to that direction (e.g., Paterson et al., 1998 for further discussion). The AMS interpretations of the lava flow and dikes can be used to help describe the development of the Sośnica Hill volcano. The AMS data show a range of flow directions that varies across the Targowica quarry yet do not yield an orderly pattern of fabric orientations (Fig. 9; Table 2). Four dikes provide paired margin data that we use to define a unique flow pattern with two sites showing upward flow, one site downward flow, and one site sub-horizontal flow (Fig. 9). Of the remaining sites, nine sites yield prolate ellipsoids and we infer shallow, subhorizontal north-south, northwest-southeast, and east-west flow directions for these dikes

based on the K1 magnetic lineation orientation. The remaining sites are of an oblate shape and yield highly scattered magnetic foliation patterns of variable strike, dip magnitudes, and dip directions across the Targowica quarry (Fig. 9). We argue that the AMS data reveal highly dynamic subsurface magma flow and emplacement directions. The magnetic fabric data arguably reflect that the Sośnica Hill volcano evolved from a polyphase feeding system and through a complex and evolving feeder network. The AMS data presented here indicate that feeder dikes bring magma in towards the central conduit and the branching dikes and sills distribute magma away from the feeder conduit towards the flanks leading to flank lava flow eruptions and pyroclastic deposits. It is conceivable that as the volcanic plumbing system evolved, magma was focused towards the central feeder conduit leading to the main volcanic eruption phase. As the cone grew, local changes to the volcanic flank structures and local stresses directed magma flow away from the central conduit edifice as further evidenced by the geophysical data and field observations within the excavated quarry. Alternatively, a decrease in magma pressure allowed magma to drain away from the conduit back into the feeder dike system and/or forceful emplacement into the pyroclastic material. Table 4 summarizes the events of the hypothesized eruptive events, magma plumbing system, magma flow beneath the Sośnica Hill volcano that is based on the AMS fabrics and the inferences derived from the paleomagnetic, geophysical, and field data. This detailed study shows that many volcanoes deserve highly detailed study, as their subtleties can provide insight into the broader crustal and magmatic environment during magmatism.

10.4. Episodic volcanism, dynamic eruptive styles, formation of various volcanic structures

The earliest activity at the Sośnica Hill volcanic system is recorded by the Lower Basalts and the Scoria Breccias and Lapillistones (Fig. 12; Table 4). These eruptive units reflect broadly contemporaneous effusive activity and explosive Strombolian-type eruptions, respectively. The Strombolian deposits are mostly massive accumulations of ballistic clasts, less commonly bedded lapillistones deposited by fall from an eruption column. At this stage of activity, basaltic lava ponded in a crater (at the present quarry site) as a lava lake fed by dikes from the north. During continuing activity, as pyroclastic material accumulated, the lava lake underwent inflation with the formation of intrusive veins in the surrounding deposits, as well as overflow lava lobes directed to the south. Pyroclastic deposits in the eastern part of the quarry were sourced from a vent in the north, inferred from a single observation of

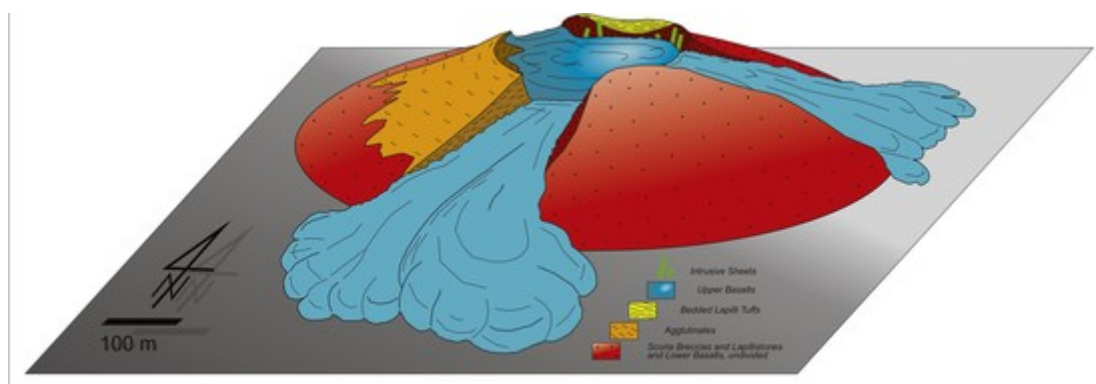


Fig. 12. Idealized structure and morphology of the Miocene Sośnica Hill volcano at the final stage of growth, as envisaged from combined geological and geophysical studies reported in this paper. The cone was mainly built of Scoria Breccias and Lapillistones with associated Lower Basalts, with smaller outcrops of Agglutinates (in the south) and Bedded Lapilli Tuffs (in the north) deposited at later stages of activity. Major lava flows developed through a breach in the southern flank during the final eruptions but smaller outflows are also found in the east and west. Intrusive Sheets were emplaced throughout the activity and provide a record of highly variable magma flow directions in the shallow level plumbing system, as well as reorientation of older dikes during the cone growth. A major lava-filled crater fed from dikes concentrated near the northern margin is depicted; however, the volcanic cone was likely more complex, with additional crater(s). The cone has been significantly eroded since Miocene (cf. Awdankiewicz, 2005). The present Targowica Quarry is located within the area of the main crater. Most of the Upper Basalts have been already quarried away and the quarry exposes, as of 2016–2020, the inner parts of the cone.

an impact sag. Inflation produced tumulus on top of the basalt flows with related formation of protrusions, breccias, local squeeze-ups of palaeohoe lobes. In addition, welded scoria reflects localized spattering, e.g. along the margins of lava lake, or from hornitoes on top of lava flows. After the emplacement of the Lower Basalts and the Scoria Breccias and Lapillistones, the activity ceased for a relatively long time and a weathered horizon/palaeosoil developed on top of the Scoria Breccias.

Among the youngest events in the evolution of the volcanic system was the eruption of the Bedded Lapilli Tuffs (Fig. 12). The Bedded Lapilli Tuffs resulted from a phreatomagmatic eruption, with some oscillations towards Strombolian-type activity. The vent was possibly located in the eastern part of the volcanic system and tephra was deposited by alternating fall and surge processes, partly burying an earlier crater/cone crest. A minor lava flow was also emplaced during this episode. As the Bedded Lapilli Tuffs and the Agglutinates with Upper Basalts are not in direct contact, their age relations remain rather equivocal. Two possible scenarios can be envisaged: (1) phreatomagmatic eruption with the deposition of the BLT preceded the Hawaiian type eruption and the formation of the WA and the UB, or (2) the opposite succession of volcanic events. Although we have no conclusive argument on that sequence, two premises are in favour of scenario (1): (i) the BLT are cut by an Intrusive Sheet (Fig. 6e, f; Fig. 12; Table 4) whereas no Intrusive Sheets cut the WA and UB, which may suggest the older age of BLT, and (ii) phreatomagmatic activity following a period of quiescence and initiating a new phase of activity is a likely evolutionary trend to be expected. Thus, a younger eruptive stage is recorded by the Agglutinates. This unit reflects an explosive Hawaiian-type activity during which a pile of hot spatter, bombs and scoria accumulated in the southern sector of the volcanic system. This pile was affected by welding and southwards directed subsidence, in a similar direction as the earlier lava flows. This suggests that a southerly directed breach was persistently present in the system. It is also possible that the eruption of the Agglutinates and of the Upper Basalts were related to the same event, which included the Hawaiian-type activity with related accumulation of spatter, bombs and scoria pile in the southern part of the system, and, contemporaneously, filling of the older crater by new lava – the Upper Basalts. In this scenario, welding and subsidence of the hot pile of Hawaiian deposits could have been aided by lateral pressure of lava in the crater (and by explosive activity?) and this caused the displacement of the southern sector of the structure, re-opening of the southern breach, and effusion of lava in that direction.

During the activity of the volcanic system, Intrusive Sheets were emplaced into the thickening succession. The intrusive sheets are not identified in the two youngest eruptive units, the Agglutinates and the Upper Basalts. The concentration of intrusive veins observed in the northern and eastern sections of the quarry as well as imaged by the electrical resistivity tomography and ground magnetometry results indicate the location of main feeders in these regions. Variable orientation of the intrusive veins, locally cross-cutting relationships, and rooting of some veins in the Lower Basalts suggest emplacement of the sheets in several episodes at various stages during the evolution of the volcanic system. Anisotropy of magnetic susceptibility data are interpreted to reflect variable flow patterns of magma in the dikes including outward and upward flow relative to the vent area, as well as inward and downward flow. In addition, paleomagnetic data reveal evidence of subvolcanic deformation of the intrusive rocks. These highly variable patterns and lack of systematic trends can be broadly linked to multiphase emplacement of the dikes controlled by dynamically changing local stress field (Fig. 12).

In a previous study (Awdankiewicz, 2005), the Sośnica Hill Volcano was considered a Strombolian scoria cone, originally 500 m - 1000 m in basal diameter and 90 m - 180 m above the paleo-land surface. The main crater was located N-NE of the quarry, a smaller vent on the western slope, and a lava-filled breach in the south. Although this interpre-

tation seems essentially correct, the new observations indicate a more complex development of the system in terms of styles of activity and structure of the final volcanic edifice. The volcanic eruptions involved Strombolian-type eruptions, phreatomagmatic explosive volcanism, and Hawaiian type eruptions. Such diversity of eruptive styles documents that the volcano is more complex than a simple, 'textbook' monogenetic scoria cone. Furthermore, the red-brown horizon likely representing fossil-weathered surface on top of Strombolian deposits evidences a longer break in activity, after which eruptions resumed with different style; this is also not typical of the simple monogenetic cones. Although the main vents can be located N to NE of the quarry, as previously considered, the lateral variation in the volcanic succession suggest eruptions from other small local vents. The complex subvolcanic magma flow patterns recorded in dikes match the variation of surface eruptive products and documents dynamically changing magma distribution paths in the near-surface, intra-cone part of the feeding system of the volcano. The inferred remnants of the inner crater wall seem to be preserved at relatively low elevations – possibly the volcanic edifice was relatively low relief, e.g. in the lower range of previously suggested values (i.e. no more than a hundred meters). The lateral variation and complexity of the succession may also indicate that the central cone and crater were less dominant than previously supposed. Possibly, the volcanic system was formed by two-three overlapping cones/craters active at successive stages, without distinct predominance of either stage.

11. Conclusions

The results from the Sośnica Hill volcano offer an exceptional example of the internal growth and magma transport mechanisms beneath a small-sized volcano, coupled with the dynamic eruptive processes at the surface level. The integration of the various field and laboratory datasets indicate five main stages involving extrusive volcanism and several intrusive events that collectively led to the development and growth of the Sośnica Hill volcano. During the extrusive stages, Strombolian-type, phreatomagmatic, and Hawaiian-type explosive eruptions occurred interspersed with phases of effusive eruptions. In the subsurface, several intrusive events of magmatism occurred involving a main pulse of dike emplacement followed by later intrusions emplaced away from the central feeder conduit(s) potentially serving as magma feeders for secondary vents along the flanks of the main cone. The presence of fossil weathering surface evidences ample time for weathering processes to have occurred between eruptions. This study demonstrates that the Sośnica Hill volcano feeder is not simply one main pipe or dike, but rather it had multiple magma conduits distributed around vent area that erupted over an extended time period. The Sośnica Hill volcanic history verges on polygenetic, spanning several hundred to thousands of years of intrusion and eruption, extending hazard periods for such activity in active volcanic centers. Many examples are found globally involving intrusive uplifts beneath a growing volcanic system involving single and multiple eruptive vents in the Central European Volcanic Province and in other monogenetic and polygenetic systems worldwide. The complex evolution and eruptive behavior, together with protracted time of the volcano activity, elucidate that small, seemingly simple volcanoes may have a very dynamic evolution involving multiple intrusive events, changing eruptive styles, and surface morphology.

Data availability

All data related to this project is available at <http://www.nmhugeology.com/>, the paleomagnetic data will be uploaded to the MagIC database (<https://www2.earthref.org/MagIC>), and all other data sets may be requested from the authors.

Author contributions

Petronis, Michael

Organized student participation in European field work related to the NSF IRES grant, partial funding support for field work, paleomagnetic, rock magnetic, and AMS data interpretation, drafting of figures, writing of the manuscript, drafting the figures, and data interpretation.

Awdankiewicz, Marek

Planning the study; providing regional geological data; field work; logging of quarry walls, characterization and interpretation of lithofacies, preparing related figures and writing related text; contribution to synthesis and interpretation of geological and geophysical results.

Valenta, Jan

Geophysical field measurements, data processing and interpretation; contributions to final synthesis; writing relevant parts of the text.

Rapprich, Vlado

Assisted with the organization of the expedition, project management, served as liaison between USA, Czech, and Polish scientists and secured partial funding to support field work.

Zebrowski, Joe

Organized all of the geospatial map making efforts, geospatial data processing (DEM and LIDAR), assisted with writing the narrative and figure drafting.

Karim, Ejaz

This work represents a large portion of Mr. Karim's Master's thesis research at New Mexico Highlands University, supervised by Petronis, Zebrowski, and Rapprich. Mr. Karim wrote an initial draft of the manuscript, figures, and data interpretation and conducted the paleomagnetic, rock magnetic, and AMS analysis as part of his Masters Thesis.

Uncited references

Fisher, 1953
Hopkinson, 1890
Knight et al., 1986
Ulrych et al., 2011

Declaration of Competing Interest

The authors declare that they have no known competing financial interests or personal relationships that could have appeared to influence the work reported in this paper.

Acknowledgements

This paper represents a major component of Ejaz Karim's Masters Thesis research at New Mexico Highlands University. This work was funded by New Mexico Highlands University Faculty Research funds, National Geographic Grant #8887-11 awarded to Petronis and Lindline, and National Science Foundation Grants #1423396 and #1658085 awarded to Petronis and Lindline. Rock magnetic (hysteresis and FORC) analysis were supported by National Science Foundation Grants DMR-1523611 and DMR-2122108 (PREM) awarded to Drs. T. Timofeeva and G. Gallegos at NMHU. The work of Rapprich contributes to the Strategic Research Plan of the Czech Geological Survey (DKRVO/ČGS 2018-2022). We acknowledge the support of the long-term conceptual development of the research organization (Awarded to J. Valenta; No. RVO: 67985891). Financial support to M. Awdankiewicz from the University of Wrocław grant KD76 is acknowledged. We thank our field assistants and laboratory assistants (Jeffrey Falance; Jose Cervantes Sandoval; Sarah Trevino) as without their efforts this project would not have been possible. All data related to this project will be made available at <http://www.nmhugeology.com/>, the paleomagnetic data will be uploaded to the MagIC database (<https://www2.earthref.org/MagIC>), FAIR principles, and all data sets may be requested from the

mspetro@nmhu.edu. Datasets for this research are included in this paper and additional data are available upon request from the authors.

References

- Applegarth, L.J., Pinkerton, H., James, M.R., Calvari, S., 2010. Morphological complexities and hazards during the emplacement of channel-fed 'a' lava flow fields: a study of the 2001 lower flow field on Etna. *Bull. Volcanol.* 72, 641–656.
- August, C., Awdankiewicz, M., Wojewoda, J., 1995. Tertiary basaltoids, volcanoclastics and sedimentary deposits in the eastern part of the Fore-Sudetic Block. *Ann. Soc. Geol. Pol. – Special Volume. LXVI Annual Meeting of Polish Geological Society. Excursion guide. Polskie Towarzystwo Geologiczne, Kraków*, pp. 241–254.
- Awdankiewicz, M., 2005. Reconstructing an eroded scoria cone: the Miocene Sońnica Hill volcano (Lower Silesia, SW Poland). *Geol. Quart.* 49 (4), 439–448.
- Awdankiewicz, M., 2013. Stop 1: Targowica, quarry of basalt. Miocene, basaltic scoria cone (structure, deposits, petrology). *Min. Spec. Pap.* 41, 97–103.
- Awdankiewicz, M., Rapprich, V., Míková, J., 2016. Magmatic evolution of compositionally heterogeneous monogenetic Cenozoic Strzelin Volcanic Field (Fore-Sudetic Block, SW Poland). *J. Geosci.* 61, 425–450.
- Babuška, V., Plomerová, J., 2001. Subcrustal lithosphere around the Saxothuringian-Moldanubian Suture zone – a model derived from anisotropy of seismic wave velocities. *Tectonophysics* 332, 185–199.
- Barde-Cabusson, S., Bolós, X., Pedrazzi, D., Lovera, R., Serra, G., Martí, J., Casas, A., 2013. Electrical resistivity tomography revealing the internal structure of monogenetic volcanoes. *Geophys. Res. Lett.* 40, 2544–2549.
- Beck, Jr., M.E., 1980. Paleomagnetic record of plate-margin tectonic processes along the western edge of North America. *J. Geophys. Res.* 85, 7115–7131.
- Besse, J., Courtillot, V., 2002. Apparent and true polar wander and the geometry of the geomagnetic field over the last 200 Myr. *J. Geophys. Res. Solid Earth* 107, 6–31.
- Birkenmajer, K., Pécskay, Z., 2002. Radiometric dating of the Tertiary volcanics in lower Silesia, Poland. I. Alkali Basaltic Rocks of the Opole Region. *Bull. Pol. Acad. Sc., Earth Sc.* 50, 31–50.
- Birkenmajer, K., Pécskay, Z., Grabowski, J., Lorenc, M.W., Zagożdźno, P.P., 2002a. Radiometric dating of the Tertiary volcanics in Lower Silesia, Poland. II. K-Ar dating and palaeomagnetic data from Neogene basanites near Łądek Zdrój, Sudetes Mts. *Ann. Soc. Geol. Pol.* 72 (2), 119–129.
- Birkenmajer, K., Pécskay, Z., Grabowski, J., Lorenc, M.W., Zagożdźno, P.P., 2002b. Radiometric dating of the Tertiary volcanics in Lower Silesia, Poland. III. K-Ar ages and palaeomagnetic data from Early Miocene basaltic rocks near Jawor, Fore-Sudetic Block. *Ann. Soc. Geol. Pol.* 72 (3), 241–253.
- Birkenmajer, K., Pécskay, Z., Grabowski, J., Lorenc, M.W., Zagożdźno, P.P., 2004. Radiometric dating of the Tertiary volcanics in lower Silesia, Poland. IV. Further K-Ar dating and palaeomagnetic data from Late Oligocene to Early Miocene basaltic rocks of the Fore-Sudetic Block. *Ann. Soc. Geol. Pol.* 74 (1), 1–19.
- Blaikie, T.N., Ailleres, L., Cas, R.A.F., Betts, P.G., 2012. Three-dimensional potential field modeling of a multi-vent maar-diatreme: the Lake Coragulac maar, Newer Volcanics Province, south-eastern Australia. *J. Volcanol. Geotherm. Res.* 235, 70–83.
- Blaikie, T.N., Ailleres, L., Betts, P.G., Cas, R.A.F., 2014. A geophysical comparison of the diatremes of simple and complex maar volcanoes, Newer Volcanics Province, south-eastern Australia. *J. Volcanol. Geotherm. Res.* 276, 64–81.
- Bolós, X., Barde-Cabusson, S., Pedrazzi, D., Martí, J., Casas, A., Himi, M., Lovera, R., 2012. Investigation of the inner structure of La Crosa de Sant Dalmat maar (Catalan Volcanic Zone, Spain). *J. Volcanol. Geotherm. Res.* 247–248, 37–48.
- Bolós, X., Barde-Cabusson, S., Pedrazzi, D., Martí, J., Casas, A., Lovera, R., Nadal-Sala, D., 2014. Geophysical exploration of the subsurface geology of La Garrotxa monogenetic volcanic field (NE Iberian Peninsula). *Int. J. Earth Sci.* 103, 2255–2269.
- Borradaile, G.J., Henry, B., 1997. Tectonic Application of magnetic Susceptibility and its Anisotropy. *Earth-Sci. Rev.* 42, 49–93.
- Büchner, J., Tietz, O., 2012. Reconstruction of the Landeskroner Scoria Cone in the Lusatian Volcanic Field, Eastern Germany – long-term degradation of volcanic edifices and implications for landscape evolution. *Geomorphology* 151, 175–187.
- Büchner, J., Tietz, O., Viereck, L., Suhr, P., Abratis, M., 2015. Volcanology, geochemistry and age of the Lausitz Volcanic Field. *Int. J. Earth Sci. (Geol. Rundsch.)* 104 (8), 2057–2083.
- Butler, R.F., 1992. *Paleomagnetism: Magnetic Domains to Geological Terranes*. Blackwell Scientific Publications, Oxford, UK 319 pp.
- Cajz, V., Rapprich, V., Erban, V., Pécskay, Z., Radoň, M., 2009. Late Miocene volcanic activity in the České středohoří Mountains (Ohře/Eger Graben, northern Bohemia). *Geol. Carpath.* 60, 519–533.
- Calvari, S., Pinkerton, H., 2004. Birth, growth and morphologic evolution of the 'Laghetto' cinder cone during the 2001 Etna eruption. *J. Volcanol. Geotherm. Res.* 132, 225–239.
- Cas, R.F., Wright, J.V., 1987. *Volcanic Successions, Modern and Ancient: A Geological Approach to Processes, Products and Successions*. Allen and Unwin, London, pp. 1–528.
- Chadima, M., Hroudá, F., 2006. Remasoft 3.0 – a user-friendly paleomagnetic data browser and analyzer. *Travaux Géophysiques XXVII*, 20–21.
- Choo, H., Song, J., Lee, W., Lee, C., 2016. Effects of clay fraction and pore water conductivity on electrical conductivity of sand-kaolinite mixed soils. *J. Pet. Sci. Eng.* 117, 735–745.
- Chulliat, A., Macmillan, S., Alken, P., Beggan, C., Nair, M., Hamilton, B., Woods, A., Ridley, V., Maus, S., Thomson, A., 2015. The US/UK World Magnetic Model for 2015–2020: Technical Report. National Geophysical Data Center, NOAA. <https://doi.org/10.7289/V5TB14V7>.
- Cwojdzinski, S., Jodłowski, S., 1982. Stained basaltic concentrations of the Bohemian

- Massif and the lower Silesia (in polish with English summary). *Biul. Inst. Geol.* 341, 201–225.
- Day, R., Fuller, M., Schmidt, V.A., 1977. Hysteresis properties of titanomagnetites: grain size and composition dependence. *Phys. Earth Planet. Inter.* 13 (4), 260–267. [https://doi.org/10.1016/0031-9201\(77\)90108-X](https://doi.org/10.1016/0031-9201(77)90108-X).
- de Goer, A., Boivin, P., Camus, G., Gourgaud, A., Kieffer, G., Mergoil, J., Vincent, P.M., 1991. *Volcanologie de la Chaîne des Puys*. Paris: Inst Geog Natl, 127 p and 1:25,000 geol map.
- Delcamp, A., Petronis, M., Troll, V., 2014. Discerning magmatic flow patterns in shallow-level basaltic dykes from the NE rift zone of Tenerife, Spain, using the Anisotropy of magnetic Susceptibility (AMS) technique. Geological Society, London, Special Publications. 396. <https://doi.org/10.1144/SP396.2>.
- Demarest, H.H., 1983. Error analysis of the determination of tectonic rotation from paleomagnetic data. *J. Geophys. Res.* 88, 4321–4328. <https://doi.org/10.1029/JB088iB05p04321>.
- Dunlop, D.J., 1972. Magnetic mineralogy of unheated and heated red sediments by coercivity spectrum analysis. *Geophys. J. Int.* 27 (1), 37–55 May 1972 <https://doi.org/10.1111/j.1365-246X.1972.tb02346.x>.
- Dunlop, D.J., 1973. Superparamagnetic and single-domain threshold sizes in magnetite. *J. Geophys. Res.* 78, 1780–1793. <https://doi.org/10.1029/JB078i011p01780>.
- Dunlop, D.J., 1981. The rock magnetism of fine particles. *Phys. Earth Planet. Inter.* 26, 1–26.
- Dunlop, D.J., 1995. Magnetism in rocks. *J. Geophys. Res.* 100 (B2), 2161–2174. <https://doi.org/10.1029/94JB026>.
- Dunlop, D.J., Özdemir, Ö., 1997. *Rock Magnetism: Fundamentals and Frontiers*. Cambridge University Press, Cambridge University Press. <https://doi.org/10.1017/CBO9780511612794>.
- Finizola, A., Revil, A., Piscitelli, S., Ricci, T., Morin, J., Angeletti, B., Mocoichian, L., Sortino, F., 2006. Hydrogeological insights at Stromboli volcano (Italy) from geoelectrical, temperature, and CO₂ soil degassing investigations. *Geophys. Res. Lett.* 33, L17304.
- Finizola, A., Ricci, T., Deiana, R., Cabusson, S.B., Rossi, M., Praticelli, N., Giocoli, A., Romano, G., Delcher, E., Suski, B., Revil, A., Menny, P., Di Gangi, F., Letort, J., Peltier, A., Villasante-Marcos, V., Douillet, G., Avard, G., Lelli, M., 2010. Adventive hydrothermal circulation on Stromboli volcano (Aeolian Islands, Italy) revealed by geophysical and geochemical approaches: implications for general fluid flow models on volcanoes. *J. Volcanol. Geotherm. Res.* 196, 111–119.
- Fisher, R.A., 1953. Dispersion on a sphere. *Proc. R. Soc. A* 217, 295–305. <https://doi.org/10.1098/rspa.1953.0064>.
- Fisher, R.V., 1966. Rocks composed of volcanic fragments and their classification. *Earth Sci. Rev.* 1 (4), 287–298.
- Flechs, C., Heinicke, J., Mrlina, J., Kämpf, H., Nickschick, T., Schmidt, A., Bayer, T., Günther, T., Rüdiger, C., Seidel, E., Seidl, M., 2015. Integrated geophysical and geological methods to investigate the inner and outer structures of the Quaternary Mýtina maar (W-Bohemia, Czech Republic). *Int. J. Earth Sci.* 104, 2087–2105.
- Foucher, M.S., Petronis, J., Lindline, B., van Wyk de Vries, 2018. Investigating the magmatic plumbing system of a Monogenetic Scoria cone: a field and laboratory study of the Cienega Scoria Cone, Cerros del Rio Volcanic Field, New Mexico. *Geochem. Geophys. Geosyst.* 19 (I. 7), 1963–1978. <https://doi.org/10.1029/2017GC007222>.
- Ghorbani, A., Revil, A., Coperey, A., Soueid, A.A., Roque, S., Heap, M.J., Grandis, H., Viveiros, F., 2018. Complex conductivity of volcanic rocks and the geophysical mapping of alteration in volcanoes. *J. Volcanol. Geotherm. Res.* 357, 106–127.
- Gunther, Mehl, F.M., Pogl, M., Zenger, C., 2006. A cache-aware algorithm for PDEs on hierarchical data structures based on space-filling curves. *SIAM J. Sci. Comput.* 28 (5), 1634–1650. <https://doi.org/10.1137/040604078>.
- Harrison, R.J., Muraszko, J., Heslop, D., Lascu, I., Muxworthy, A.R., Roberts, A.P., 2018. An improved algorithm for unmixing first-order reversal curve diagrams using principal component analysis. *Geochem. Geophys. Geosyst.* 19, 1595–1610. <https://doi.org/10.1029/2018GC007511>.
- Hasan, M.F., Abuel-Naga, H., Broadbridge, P., Leong, E.C., 2018. Series-parallel structure-oriented electrical conductivity model of saturated clays. *Appl. Clay Sci.* 162, 239–251.
- Heider, F., Dunlop, D.J., Sugiura, N., 1987. Magnetic properties of hydrothermally recrystallized magnetite crystals. *Science* 236 (4806), 1287–1290. <https://doi.org/10.1126/science.236.4806.1287>.
- Hintz, A., Valentine, G., 2012. Complex plumbing of monogenetic scoria cones: new insights from the Lunar Crater Volcanic Field (Nevada, USA). *J. Volcanol. Geotherm. Res.* 239, 19–32.
- Holub, F.V., Rappich, V., Erban, V., Peesky, Z., Mlčoch, B., Mikova, J., 2010. Petrology and geochemistry of the Tertiary alkaline intrusive rocks at Doupov, Doupovské hory Volcanic complex (NW Bohemian Massif). *J. Geosci.* 55, 251–278.
- Hopkinson, J., 1890. Magnetic properties of alloys of nickel and iron. *Proc. R. Soc. Lond.* 48, 1–13.
- Hrouda, F., 1982. Magnetic anisotropy of rocks and its applications in geology and geophysics. *Geophys. Surv.* 5, 38–82.
- Jeffery, G., 1922. The motion of ellipsoidal particles immersed in a viscous fluid. *Proc. R. Soc. Lond. A* 102, 201–211.
- Jelinek, V., 1981. Characterization of the magnetic fabric of rocks. *Tectonophysics* 79, 63–70.
- Johnson, N.M., Opdyke, N.D., Lindsay, E.H., 1975. Magnetic polarity stratigraphy of Pliocene–Pleistocene terrestrial deposits and vertebrate faunas, San Pedro Valley, Arizona. *Geol. Soc. Am. Bull.* 86, 5–12.
- Kereszturi, G., Németh, K., 2012. Monogenetic basaltic volcanoes. Genetic classification, growth, geomorphology and degradation.
- Khan, M.A., 1962. The anisotropy of magnetic susceptibility of some igneous and metamorphic rocks. *J. Geophys. Res. Solid Earth* 67 (7), 2873–2885. <https://doi.org/10.1029/JZ067i007p02873>.
- Kirschvink, J.L., 1980. The least-square line and plane and the analysis of paleomagnetic data. *Geophys. J. R. Astron. Soc.* 62, 699–718.
- Knight, M.D., Walker, G.P.L., 1988. Magma flow directions in dikes of the Koolau complex, Oahu, determined from magnetic fabric studies. *J. Geophys. Res.* 93, 4301–4309.
- Knight, M.D., Walker, G.P.L., Ellwood, B.B., Diehl, J.F., 1986. Stratigraphy, paleomagnetism, and magnetic fabric of the Toba Tuffs: constraints on the sources and eruptive styles. *J. Geophys. Res.* 91, 10355–10382.
- Kościółko, H., Morawski, T., Sikora, W.S., 1986. Smectites of hydrothermal origin in rocks of the basaltic formation of lower Silesia (in Polish with English summary). *Arch. Mineral.* 41 (1), 19–29.
- Kozłowska-Koch, M., 1987. Classification and nomenclature of the Tertiary volcanic rocks of the Low- and Opole Silesia (in polish with English summary). *Arch. Mineral.* 42 (1), 43–95.
- Le Maitre, R.W., (ed), Streckeis, A., Zanettin, B., Le Bas, M.J., Bonin, B., Bateman, P., Bellieni, G., Dudek, A., Efremova, S., Keller, J., Lameyre, J., Sabine, P.A., Schmid, R., Sørensen, H., Wooley, A.R., 2002. *Igneous Rocks. A Classification and Glossary of Terms. Recommendations of the International Union of Geological Sciences Subcommittee on the Systematics of Igneous Rocks*. 2nd edition Cambridge University Press, Cambridge–New York, pp. 1–193.
- Lichoro, C.M., Arnason, M., Cumming, W., 2019. Joint interpretation of gravity and resistivity data from the Northern Kenya volcanic rift zone: structural and geothermal significance. *Geothermics* 77, 139–150.
- Loke, M.H., Barker, R.D., 1996. Rapid least-squares inversion of apparent resistivity pseudosections by a quasi-Newton method. *Geophys. Prospect.* 44, 131–152.
- Lowrie, W., Fuller, M., 1971. On the alternating field demagnetization characteristics of multidomain thermoremanent magnetization in magnetite. *J. Geophys. Res.* 76, 6339–6349.
- Luhr, J.F., Simkin, T., 1993. *Paricutin: The Volcano Born in a Mexican Cornfield* 427 pp Phoenix, Arizona.
- Lustrino, M., Wilson, M., 2007. The Circum-Mediterranean anorogenic Cenozoic igneous province. *Earth Sci. Rev.* 81, 1–65.
- Marshall, A., Connor, C., Kruse, S., Malservisi, R., Richardson, J., Courtland, L., Connor, L., Wilson, J., Karegar, M.A., 2015. Subsurface structure of a maar–diatreme and associated tuff ring from a high-resolution geophysical survey, Rattlesnake Crater, Arizona. *J. Volcanol. Geotherm. Res.* 304, 253–264.
- Matte, P., 1986. Tectonics and plate tectonics for the Variscan belt in Europe. *Tectonophysics* 137 (1), 31–42.
- Mazur, S., Aleksandrowski, P., Kryza, R., Oberc-Dziedzic, T., 2006. The Variscan Orogen in Poland. *Geol. Q* 50, 89–118.
- McPhie, J., Doyle, M., Allen, R., 1993. *Volcanic Textures. A Guide to the Interpretation of Textures in Volcanic Rocks*. CODES, Tasmania 198 pp.
- Merrill, R.T., McElhinny, M.W., 1983. *The Earth's Magnetic Field*. Academic Press, London.
- Mertes, H., Schmincke, H.U., 1985. Mafic potassic lavas of the Quaternary West Eifel volcanic field. *Contrib. Mineral. Petrol.* 89, 330–334.
- Migoń, P., Pijet-Migoń, E., 2016. Overlooked geomorphological component of volcanic geoheritage – diversity and perspectives for tourism industry, Pogórze Kaczawskie Region, SW Poland. *Geoheritage* 8, 333–350.
- Mlčoch, B., Konopásek, J., 2010. Pre-late Carboniferous geology along the contact of the Saxothuringian and Teplá-Barrandian zones in the area covered by younger sediments and volcanics (western Bohemian Massif, Czech Republic). *J. Geosci.* 55 (2), 81–94.
- Moskowitz, B.M., 1981. Methods for estimating Curie temperatures of titanomagnetites from experimental Js-T data. *Earth Planet. Sci. Lett.* 53 (1), 84–88. [https://doi.org/10.1016/0012-821X\(81\)90028-5](https://doi.org/10.1016/0012-821X(81)90028-5).
- Németh, K., 2010. Monogenetic volcanic fields: Origin, sedimentary record, and relationship with polygenetic volcanism. In: *What Is a Volcano?* GSA Special Paper, Vol. 470, p. 43.
- Oldenburg, D.W., Yaoguo, L., 1999. Estimating depth of investigation in dc resistivity and IP surveys. *Geophysics* 64, 403–416.
- Paterson, S.R., Fowler, J.R.T.K., Schmidt, K.L., Yoshinobu, A.S., Yuan, E.S., Miller, R.B., 1998. Interpreting magmatic fabric patterns in plutons. *Lithos* 44, 53–82.
- Peccerillo, A., Frezzotti, M.L., De Astis, G., Ventura, G., 2006. Modeling the magma plumbing system of Vulcano (Aeolian Islands, Italy) by integrated fluid-inclusion geobarometry, petrology, and geophysics. *Geology* 34, 17–20.
- Petronis, M.S., Delcamp, A., van Wyk de Vries, B., 2013. Magma emplacement into the Lemptégy scoria cone (Chaîne Des Puys, France) explored with structural, anisotropy of magnetic susceptibility, and Paleomagnetic data. *Bull. Volcanol.* 75, 1–22.
- Petronis, M.S., Brister, A.R., Rappich, V., van Wyk de Vries, B., Lindline, J., Mišurec, J., 2015. Emplacement history of the Trosky basaltic volcano (Czech Republic): paleomagnetic, rock magnetic, petrologic, and anisotropy of magnetic susceptibility evidence for lingering growth of a monogenetic volcano. *J. Geosci.* 60, 129–147.
- Petronis, M.S., Valenta, J., Rappich, V., Lindline, J., Shields, S., van Wyk de Vries, B., Heizler, M., Balek, J., Fojtíková, L., Táborík, P.R., 2018. Emplacement history of the Miocene Zebín Tuff Cone (Czech Republic) revealed from ground geophysics, anisotropy of magnetic susceptibility, paleomagnetic, and 40Ar/39Ar geochronology data. *Geochem. Geophys. Geosyst.* 19 (10), 3764–3792. <https://doi.org/10.1029/2017GC007324>.
- Pike, C.R., Roberts, A.P., Verosub, K.L., 1999. Characterizing interactions in fine magnetic particle systems using first order reversal curves. *J. Appl. Phys.* 85, 6660–6666.
- Pike, C.R., Roberts, A.P., Dekkers, M.J., Verosub, K.L., 2001. An investigation of multidomain hysteresis mechanisms using FORC diagrams. *Phys. Earth Planet. Inter.* 126 (1–2), 11–25. [https://doi.org/10.1016/S0031-9201\(01\)00241-2](https://doi.org/10.1016/S0031-9201(01)00241-2).
- Prezzi, C., Rizzo, C., Orgeira, M.J., Nullo, F., Sigismondi, M.E., Margonari, L., 2017. Subsurface architecture of Las Bombas volcano circular structure (Southern Mendoza, Argentina) from geophysical studies. *J. S. Am. Earth Sci.* 77, 247–260.

- Rapprich, V., Holub, F.V., 2008. Geochemical variations within the Upper Oligocene–Lower Miocene lava succession of Uhost Hill (NE margin of Doupovské hory Mts., Czech Republic). *Geol Q* 52, 253–268.
- Rapprich, V., Cajz, V., Košťálek, M., Pěcský, Z., Řídkošil, T., Raška, P., Radoň, M., 2007. Reconstruction of eroded monogenic Strombolian cones of Miocene age: a case study on character of volcanic activity of the Jičín Volcanic Field (NE Bohemia) and subsequent erosional rates estimation. *J. Geosci.* 52, 169–180.
- Rapprich, V., Shields, S., Halodová, P., Lindline, J., van Wyk de Vries, B., Petronis, M.S., Valenta, J., 2017. Fingerprints of magma–mingle processes within the monogenetic Zebín tuff-cone feeding system (Jičín Volcanic Field, Czech Republic). *Journal of Geosciences; Prague Vol. 62. Iss. 4 (2017)*, 215–229. <https://doi.org/10.3190/jgeosci.245>.
- Rapprich, V., Valenta, J., Brož, M., Kadlecová, E., van Wyk de Vries, B., Petronis, M.S., Rojčík, P.A., 2019. Crucial site in the argument between neptunists and plutonists: reopening of the historical adit in the Komorná hůrka (Kammerbühl) Volcano after 180 years. *Geohéritage* 11, 347–358.
- Reynolds, J.M., 2011. *An Introduction to Applied and Environmental Geophysics*. 2nd ed. Wiley-Blackwell, Chichester, UK, 978-0-471-48535-3.
- Richter, C., van der Pluijm, B.A., 1994. Separation of paramagnetic and ferrimagnetic susceptibilities using low temperature magnetic susceptibilities and comparison with high field methods. *Phys. Earth Planet. Inter.* 82 (2), 113–123.
- Roberts, A.P., Pike, C.R., Verosub, K.L., 2000. Firstorder reversal curve diagrams: a new tool for characterizing the magnetic properties of natural samples. *J. Geophys. Res.* 105, 28,461–28,475.
- A.P. Roberts T.P. Almeida N.S. Church R.J. Harrison D. Heslop Y. Li ... X. Zhao Resolving the origin of pseudo-single domain magnetic behavior *J. Geophys. Res. Solid Earth* 122 2017 9534 9558 <https://doi.org/10.1002/2017JB014860>
- Rowland, S.K., Walker, G.P., 1987. Toothpaste lava: characteristics and origin of a lava structural type transitional between pahoehoe and aa. *Bull. Volcanol.* 49 (4), 631–641.
- Rowland, S.K., Walker, G.P., 1990. Pahoehoe and aa in Hawaii: volumetric flow rate controls the lava structure. *Bull. Volcanol.* 52 (8), 615–628.
- Rücker, C., Günther, T., Spitzer, K., 2006. Three-dimensional modeling and inversion of dc resistivity data incorporating topography – I. modelling. *Geophys. J. Int.* <https://doi.org/10.1111/j.1365-246X.2006.03010.x>.
- Sawicki, L. (Ed.), 1967. *Geological Map of the Lower Silesia Region 1:200000 (without Quaternary)*. Instytut Geologiczny, Warszawa (in Polish).
- Schmidt, A., Nowaczyk, N., Kämpf, H., Schüller, I., Flechsig, C., Jahr, T., 2013. Origin of magnetic anomalies in the large Ebersbrunn diatreme, W Saxony, Germany. *Bull. Volcanol.* 75, 1–18.
- Schmincke, H.U., 2004. *Volcanism*. Springer-Verlag, Berlin/Heidelberg 324 pp.
- Sigurdsson, H., Houghyon, B., McNutt, S.R., Rymer, H., 2000. *Encyclopedia of Volcanoes*. Acad. Press.
- Skácelová, Z., Rapprich, V., Valenta, J., Hartvich, F., Šrámek, J., Radoň, M., Gaždová, R., Nováková, L., Kolínský, P., Pěcský, Z., 2010. Geophysical research on structure of partly eroded maar volcanoes: Miocene Hnojnice and Oligocene Rychnov volcanoes (northern Czech Republic). *J. Geosci.* 55, 333–345.
- Skála, R., Ulrych, J., Ackerman, L., Jelinek, E., Dostál, J., Hegner, E., Řanda, Z., 2014. Tertiary alkaline Roztoky Intrusive Complex, České Středohoří Mts., Czech Republic: petrogenetic characteristics. *Int. J. Earth Sci. (Geol Rundsch)* 103, 1233–1262.
- Tabbagh, A., Cosenza, P., 2007. Effect of microstructure on the electrical conductivity of clay-rich systems. *Phys. Chem. Earth* 32, 154–160.
- Tarling, D.H., Hrouda, F., 1993. *The Magnetic Anisotropy of Rocks*. Chapman and Hall, London 222 pp.
- Tauxe, L., 1998. *Paleomagnetic Principles and Practice*, vol. 17 of modern approaches in geophysics. Kluwer, Dordrecht 316 pp.
- Tietz, O., Büchner, J., 2015. The landscape evolution of the Lausitz Block since the Palaeozoic—with special emphasis to the neovolcanic edifices in the Lausitz Volcanic Field (Eastern Germany). *Zeit Deutsch Gesell Geowiss* 166, 125–147.
- Torrese, P., Pozzobon, R., Rossi, A.P., Unnithan, V., Sauro, F., Borrmann, D., lauterbach H., Santagata T., 2021. Detection, imaging and analysis of lava tubes for planetary analogue studies using electric methods (ERT). *Icarus* 357, 114244.
- Udphuay, S., Günther, T., Everett, M.E., Warden, R.R., Briaud, J.-L., 2011. Three-dimensional resistivity tomography in extreme coastal terrain amidst dense cultural signals: application to cliff stability assessment at the historic D-Day site. *Geophys. J. Int.* 185, 201–220.
- Ulrych, J., Dostál, J., Adamovič, J., Jelinek, E., Špaček, P., Hegner, E., Balogh, K., 2011. Recurrent Cenozoic volcanic activity in the Bohemian Massif (Czech Republic). *Lithos* 123, 133–144.
- Urrutia-Fucugauchi, J., Trigo-Huesca, A., Pérez-Cruz, L., 2012. Magnetic links among lava flows, tuffs and the underground plumbing system in a monogenetic volcano, derived from magnetics and paleomagnetic studies. *Phys. Earth Planet. Inter.* 212–213, 10–18.
- Valenta, J., Rapprich, V., Skácelová, Z., Gaždová, R., Fojtíková, L., 2014a. The newly discovered Neogene maar volcano near the Mariánské Lázně, Western Bohemia. *Acta Geodyn. Geomater.* 11, 107–116.
- Valenta, J., Rapprich, V., Stárková, M., Skácelová, Z., Fojtíková, L., Staňek, F., Bálek, J., 2014b. Problems and challenges in detection of pre-Mesozoic maar volcanoes: example from the Principálek Volcano in the Permian Krkonoše Piedmont Basin. *J. Geosci.* 59, 169–181.
- Wilson, M., Downes, H., 1991. Tertiary—Quaternary extension-related alkaline magmatism in western and Central Europe. *J. Petrol.* 32 (4), 811–849.
- Wilson, M., Downes, H., 2006. Tertiary-Quaternary intra-plate magmatism in Europe and its relationship to mantle dynamics. *Geol. Soc. Lond. Mem.* 32 (1), 147–166.
- Wilson, M., Downes, H., Cebria, J.M., 1995. Contrasting fractionation trends in coexisting continental alkaline magma series, Cantal, Massif Central, France. *J. Petrol.* 36, 1729–1753.
- Wood, C.A., 1980. Morphometric evolution of cinder cones. *J. Volcanol. Geotherm. Res.* 7, 387–413.
- Žák, J., Tomek, F., Vacek, F., Kachlík, V., Svojtka, M., Ackerman, L., Ježek, J., Petronis, M. S., 2021. Distributed Crustal Shortening Followed by Transpressional Shearing in the Superior Province, Northeastern Canada: A Late Archean Analogy to Modern Accretionary Plate Margins?. (In press *Precambrian Research XXXX*).
- Zijderveld, J.D.A., 1967. A.C. Demagnetization of rocks: analysis of results. In: Collinson, D.W., Creer, K.M., Runcorn, S.K. (Eds.), *Methods in Paleomagnetism*. Elsevier, Amsterdam 254, 286.